LITHOS 398-399 (2021) 106348

Contents lists available at ScienceDirect

LITHOS

journal homepage: www.elsevier.com/locate/lithos

Mantle melting models of the Kızıldağ ophiolite in SE Turkey: Two types of partial melting processes in the oceanic upper mantle of southern Neo-Tethys

Chen Chen [a,b,*], Ben-Xun Su [b,c], Christina Yan Wang [a], İbrahim Uysal [d], Zhuo-Sen Yao [e]

[a] Key Laboratory of Mineralogy and Metallogeny, Guangzhou Institute of Geochemistry, Chinese Academy of Sciences, Guangzhou 510460, China
[b] Key Laboratory of Mineral Resources, Institute of Geology and Geophysics, Chinese Academy of Sciences, Beijing 100029, China
[c] University of Chinese Academy of Science, Beijing 100049, China
[d] Department of Geological Engineering, Karadeniz Technical University, 61080 Trabzon, Turkey
[e] Department of Earth Sciences, Carleton University, Ottawa, ON K1S 5B6, Canada

ARTICLE INFO

Keywords:
Kızıldağ ophiolite
Forearc basalt
Boninitic melt
Polybaric continuous melting
Flux-melting

ABSTRACT

Many ophiolites in southern Neo-Tethys contain complete lithologic sequences, with the dikes and lavas commonly having highly variable geochemical compositions. In this study, we examine the sheeted dikes and layered and isotropic gabbros of the Kızıldağ ophiolite (southern Turkey) and suggest that the compositional variations of the rocks are likely related to melting models of the mantle. The sheeted dikes and gabbros of the ophiolite have $^{206}Pb/^{204}Pb_{(90\ Ma)}$ of 17.765–19.361, $^{207}Pb/^{204}Pb_{(90\ Ma)}$ of 15.570–15.665 and $^{208}Pb/^{204}Pb_{(90\ Ma)}$ of 37.812–39.269, straddling the fields of Indian Ocean MORB and modern marine sediments. The sheeted dikes have low rare earth element (REE) concentrations and La_N/Yb_N ratios (e.g., Yb < 2.5 ppm and La_N/Yb_N of 0.33 to 0.62 on average), comparable with those of forearc basalt (FAB), except for a few samples whose trace element concentrations and patterns are similar to those of boninite. All the studied samples have positive anomalies of large ion lithophile elements (LILE) (e.g., Rb, Ba, Th, U and Sr) on a N-MORB-normalized trace element diagram and show considerable scatter on the plot of Th/Yb vs. Nb/Yb, which is attributed to involvement of slab-derived melts/fluids in a protoarc-forearc setting. Thermodynamic modelling results suggest that the parental magmas of the sheeted dikes were combined melts derived by both polybaric continuous melting (<10%) and flux-melting (<25%) of the mantle wedge during subduction initiation. In contrast, clinopyroxene and plagioclase in the layered and isotropic gabbros have compositions similar to those of boninite. The gabbro compositions can be simulated by batch crystallization of the boninitic melts, and the relatively high trace element concentrations of some isotropic gabbros likely reflect a high fraction of interstitial liquid in the crystal mush. Thus, we propose that the compositional variations of the sheeted dikes reflect two types of mantle melting, and that the gabbros were produced by subsequent crystallization within a crystal mush having variable fractions of interstitial liquid. Not only can such complex magmatic processes explain the observed compositional variations of dikes and lavas of the Kızıldağ ophiolite, but may be appliable to other ophiolites in southern Neo-Tethys, such as the Lycian, Pozantı-Karsantı and Troodos massifs.

1. Introduction

Tethyan ophiolites are widely accepted to be fragments of oceanic lithosphere generated in suprasubduction zone (SSZ) settings (e.g., Dilek and Flower, 2003; Dilek and Furnes, 2009; Parlak et al., 2002; Uysal et al., 2018). Many studies have shown that the lavas, sheeted dikes, and gabbros of these ophiolites have compositions ranging from boninite and island arc tholeiite (IAT) to MORB-like basalt (e.g., Beccaluva et al., 2004; Dilek et al., 2005, 2007, 2008; Dilek and Thy, 2009; Ishikawa et al., 2002). Such highly variable compositions are thought to be linked to the nature of their mantle sources (e.g., Kelemen et al., 1995; Kimura, 2017; Lee et al., 2009). For example, the Geotimes lavas of the Semail

* Corresponding author at: Key Laboratory of Mineralogy and Metallogeny, Guangzhou Institute of Geochemistry, Chinese Academy of Sciences, Guangzhou 510460, China.
E-mail address: chenchen2@gig.ac.cn (C. Chen).

https://doi.org/10.1016/j.lithos.2021.106348
Received 12 December 2020; Received in revised form 23 June 2021; Accepted 5 July 2021
Available online 8 July 2021

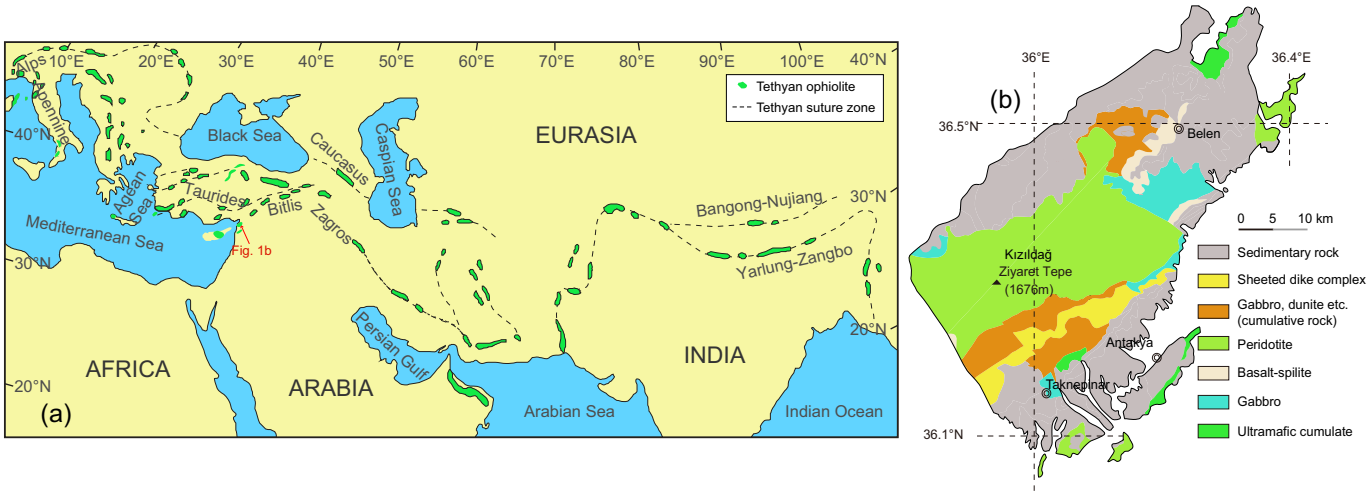

Fig. 1. (a) Distribution of the Tethyan ophiolites (Su et al., 2020). (b) Geological sketch map of the Kızıldağ ophiolite (modified after Dilek and Thy, 2009).

ophiolite (Oman) have MORB-like compositions, which are thought to have been generated by partial melting of depleted MORB mantle (DMM) (Godard et al., 2006), whereas the mafic rocks of the Mirdita ophiolite are characterized by high Th/Yb and low Nb/Yb ratios, which are attributed to derivation from a depleted mantle source metasomatized by slab-derived fluids (Dilek and Furnes, 2009). In addition to variations in mantle source composition, the geochemical diversity of magma within SSZ ophiolites may also reflect variations in other controlling factors, such as pressure (P), temperature (T), and partial melting mechanisms. Thus far, most studies on SSZ ophiolites have focused on geochemical affinities (e.g., the element ratios and patterns) between the mafic rocks and the natures of primary or modified mantle sources, which only provide a qualitative understanding of melt evolutions in ophiolites (e.g., Bagci et al., 2008; Bingol et al., 2018; Dilek and Thy, 2009; Kakar et al., 2015).

In order to gain a more quantitative understanding of partial melting processes during the formation of SSZ ophiolites, several studies have attempted to calculate the variations of concentrations and ratios of trace elements in magmas produced by different melting mechanisms, including adiabatic decompression melting, polybaric continuous melting, or even non-modal batch melting without any consideration of the P-T melting path (e.g., Khedr et al., 2014; Lian et al., 2017; Saccani et al., 2014; Sayit et al., 2016). Models based on adiabatic decompression melting, and non-modal batch melting were commonly used in previous studies (e.g., Lian et al., 2017; Sayit et al., 2016). The prerequisite for both models is that the melts should be always have been in equilibrium with the host mantle along the entire melting path (Lee et al., 2009; Yao et al., 2018), and that the fraction of melt and mineral phases in the non-modal melting should remain fixed (e.g., Lee et al., 2012; Sayit et al., 2016). Unfortunately, such constraints are likely inconsistent with the actual melting processes in SSZ mantle. On the other hand, it is generally agreed that flux-melting of a mantle wedge is the major melting mechanism in subduction zones (e.g., Grove et al., 2012; Stern, 2002; Tatsumi and Eggins, 1995), although decompression-

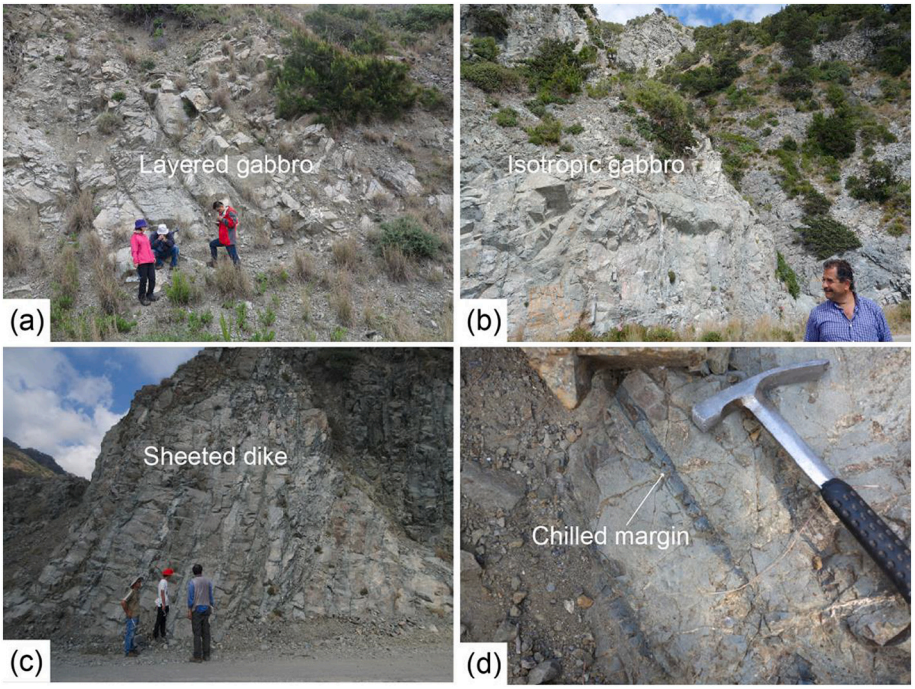

Fig. 2. Field outcrops of mafic rocks in the Kızıldağ ophiolite. (a) Layered gabbros. (b) Isotropic gabbros. (c) Sheeted dikes. (d) Chilled margins on the sheeted dikes.

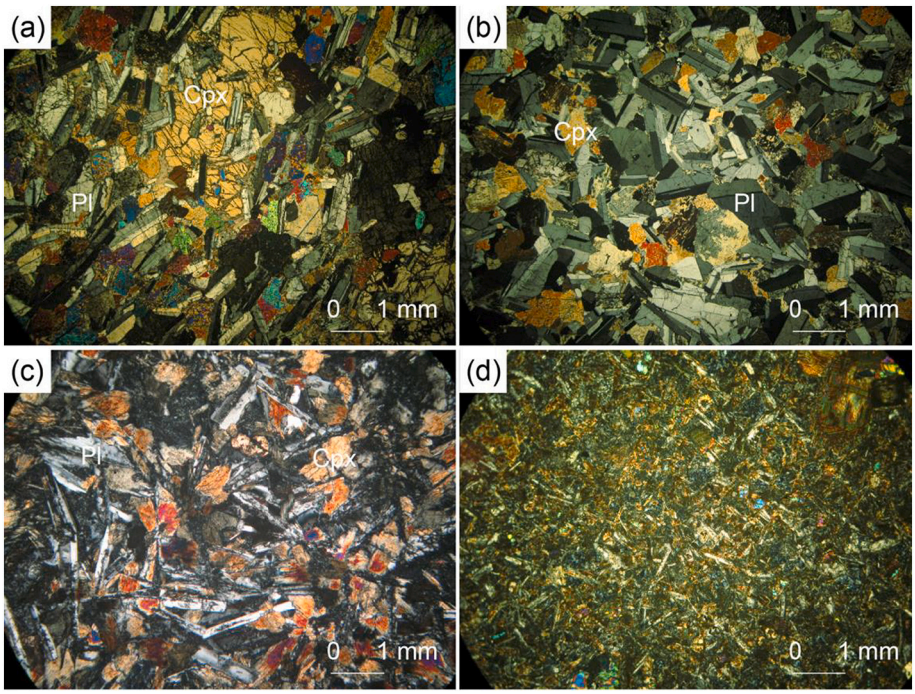

Fig. 3. Photomicrographs of the layered gabbro, isotropic gabbro, and sheeted dikes from the Kızıldağ ophiolite. (a, b) Adcumulate texture in layered gabbro with planar lamination of tabular plagioclase and subhedral clinopyroxene/orthopyroxene. (c) Ophitic texture in isotropic gabbro. (d) Micro-ophitic texture in a sheeted dike. Abbreviations: Cpx, clinopyroxene; Pl, plagioclase.

induced melting (polybaric continuous melting) may also play a significant role in some cases (Behn et al., 2011; Cooder et al., 2002; Kohut et al., 2006; Lee et al., 2009). However, we note that the model based on flux-melting of the mantle has rarely been applied to SSZ ophiolites (e.g., Dilek and Furnes, 2019). Mantle wedges above subduction zones may have undergone long-term, multiple interactions with slab-derived melts/fluids (Stern, 2002), which would have triggered partial melting of the mantle. In addition, the final melts produced by flux-melting of the mantle wedge are related to the physical parameters and the thermal states of the subduction zones (Lee et al., 2009), both of which can be highly variable. In this study, we firstly estimated the pressures and temperatures of melting processes based on new silica activity thermobarometers (Lee et al., 2009). Using these data, we then simulated the compositional variations of the melts derived from flux-melting using the assumed compositions of starting mantle sources and slab-derived melts/fluids (Kimura, 2017) and the alphaMELTS thermodynamic software (Smith and Asimow, 2005).

We selected the Kızıldağ ophiolite in southern Turkey for this study because it preserves a complete profile of a SSZ ophiolite (Chen et al., 2015, 2019) and has been suggested to contain both MORB-like lavas and IAT sequences (Dilek and Thy, 2009). To address the problem, we used two end-member models, i.e., polybaric continuous melting and flux-melting of the mantle wedge, to simulate the mantle melting processes in the generation of the sheeted dikes, and the subsequent crystallization processes by which the layered and isotropic gabbros were formed. Our models clearly suggest that the highly variable compositions of the lavas in the southern Tethyan ophiolites could be the integrated results of two types of partial melting processes in the mantle source.

2. Geological setting and sample description

Ophiolites are widely distributed in the Alpine-Himalayan orogenic belt, particularly in the eastern Mediterranean region. The latter, which crop out from Greece through Turkey to northwest Syria and into Iran and Oman, are widely recognized as SSZ-type ophiolites (e.g., Lytwyn and Casey, 1993; Robertson, 2002). Those in southern Turkey mainly crop out in two belts, the Tauride belt and Peri-Arabic belt (Dilek and Moores, 1990; Parlak et al., 1996). Ophiolites along the Tauride active margin, include the Lycian, Antalya, Beyşehir, Ali Hoca, Mersin and Pozantı-Karsantı massifs (Chen et al., 2018; Dilek and Moores, 1990); those in the Peri-Arabic belt include the Troodos ophiolite in Cyprus, Bear-Bassit ophiolite in Syria, Kızıldağ and Guleman ophiolites in Turkey, Zagros ophiolite in Iran and the Semail ophiolite in Oman (Dilek and Moores, 1990; Ricou et al., 1984).

The Kızıldağ ophiolite is ~25 km wide, ~45 km long, up to 7 km thick, and crops out over an area of ~950 km^2 (Chen et al., 2015; Lytwyn and Casey, 1993). The complete sequence includes, from the base upward, mantle tectonites, ultramafic-mafic cumulates, sheeted dikes, plagiogranites and lavas (Fig. 1) (Bagci et al., 2008). The mantle tectonites, which are 3 km thick, consist mainly of harzburgite with local lenses and bands of dunite, all intruded by pegmatitic gabbroic and pyroxenitic dikes (Dilek and Thy, 1998). The ultramafic-mafic cumulates are composed of dunite, lherzolite, wehrlite, and websterite, accompanied by layered and isotropic gabbro (Fig. 2a, b). The ~2.5-km-thick sequence of isotropic gabbro occurs directly above the ultramafic-mafic cumulates (Piskin et al., 1990; Tinkler et al., 1981) (Fig. 2b), and is, in turn, overlain by an ~1.5-km-thick sequence of sheeted dikes with well-preserved one- and two-sided chilled margins (Bagci et al., 2008; Karaoğlan et al., 2013) (Fig. 2c, d). The sheeted dikes extend E-W along strike and are exposed in an area of 60 km^2 (Bagci et al., 2008). At least three generations of dikes are recognized on the basis of cross-cutting relationships, textures and compositions (Dilek and Thy, 1998). Overlying the dikes is a sequence of pillow basalts and massive lava flows (Lytwyn and Casey, 1993). The parental magmas of the lavas vary in composition from IAT to low-Ti boninitic varieties (Bagci et al., 2008). The plagiogranites and gabbros have been dated to be 91 ± 1.9 Ma and 91.6 ± 3.8 Ma, respectively (Karaoğlan et al., 2013), and are considered to have been emplaced in the pre-Maastrichtian (Karaoğlan et al., 2013).

The layered gabbro is composed of plagioclase (40–55 vol%), clinopyroxene (25–40 vol%), and orthopyroxene (<15 vol%) with minor amounts of opaque minerals. Plagioclase laths range in size from 0.4 mm

to 2 mm, and some are enclosed within clinopyroxene oikocrysts. Plagioclase laths and subhedral clinopyroxene/orthopyroxene crystals show planar lamination (Fig. 3a, b).

The isotropic gabbro is equigranular with an ophitic texture. Typical samples consist of plagioclase laths (55–70 vol%) and interstitial, subhedral grains of clinopyroxene (30–45 vol%) (Fig. 3c). All minerals in the isotropic gabbros are typically <1.5 mm in size, smaller than those of the layered gabbros.

The sheeted dikes consist mainly of diabase and microdiorite with ophitic, subophitic and microlitic textures. Plagioclase is euhedral to subhedral with grain sizes <1 mm and is randomly oriented. Anhedral clinopyroxene ranges in size from 0.05 to 0.9 mm (Fig. 3d). Both clinopyroxene and hornblende are locally altered to fibrous actinolite.

3. Analytical methods

3.1. Mineral major element analyses

Major element compositions of minerals were determined by wavelength-dispersive X-ray spectrometry using a JEOL JXA8100 electron probe microanalyzer at the Institute of Geology and Geophysics, Chinese Academy of Sciences (IGGCAS). The analyses were carried out with an accelerating voltage of 15 kV, 10 nA beam current, 5 μm beam spot and 10–30s peak counting time. Natural minerals and synthetic phases were used as reference materials for calibration; jadeite ($NaAlSi_2O_6$) for Na, Al and Si; rhodonite ($Mn_5Si_5O_{15}$) for Mn; sanidine ($KAlSi_3O_8$) for K; garnet ($Fe_3Al_2Si_3O_{12}$) for Fe; Cr-diopside [$(Mg,Cr)CaSi_2O_6$] for Ca; olivine [$(Mg,Fe)_2SiO_4$] for Mg; rutile for Ti; Cr_2O_3 for Cr; and Ni_2Si for Ni. A software program based on the atomic number absorption fluorescence was used for matrix corrections. Typical analytical uncertainty for all elements analyzed was better than 1.5%.

3.2. Whole-rock major oxides and trace element analyses

Whole-rock major oxides were analyzed using X-ray fluorescence spectrometry (XRF) on fused glass discs prepared from a mixture of about 0.5 g of sample powder and 5 g of $Li_2B_4O_7$. The discs were analyzed on an AXIOS Mineral Spectrometer at IGGCAS. Before preparing the discs, loss on ignition (LOI) was determined by the weight difference before and after high temperature (1000 °C) calcinations of the rock power. Standard GSR-1 was used for calibration. The 95% confidence limits for the analysis were ± 0.04% to ± 0.05% for SiO_2 and Al_2O_3, and ± 0.01% to ± 0.02% for the other major oxides (MgO, Na_2O, K_2O, TiO_2, MnO and CaO).

Whole-rock trace elements were determined by inductively coupled plasma mass spectrometry (ICP-MS) at IGGCAS, using an Agilent 7500a system after digestion of the samples in a mixture of ultra-pure HF and HNO_3 in Teflon bombs. GSR, a basalt reference material, was analyzed along with unknown samples to check for instrument drift. Analyses of standards (GSR-1 and GSR-3) indicate that the precision (RSD) was better than 3% for all of trace elements measured.

3.3. Whole-rock Pb isotope analyses

About 100-120 mg of rock powder were completely decomposed with a mixture of HF-HNO_3 in Savillex Teflon screw-cap beakers at 160 °C for seven days. The Pb fraction with high purity was separated from the rock matrix using an HBr-HCl elution procedure on Teflon columns containing ~0.15 ml of anion resin (AG1-X8, 100-200 mesh). Whole procedural blanks of Pb were approximately 200 pg. The high-purity Pb fraction was re-dissolved using a mixture of silica gel and H_3PO_4 and loaded onto a single-Re filament. Pb isotopic ratio determinations were performed on a ThermoFisher Triton Plus multi-collector thermal ionization mass spectrometer at IGGCAS. International standard NIST 981 was used to monitor instrument stability during the period of data collection and to correct for mass fractionation

Table 1
Major oxide compositions (wt%) of clinopyroxene of the gabbro and sheeted dike samples from the Kızıldağ ophiolite.

Sample	Rock type	Mineral	SiO_2	TiO_2	Al_2O_3	FeO	MnO	MgO	CaO	Na_2O	K_2O	Cr_2O_3	Total	Fs	Wo	En	Mg#	Ti(M1)	Al^{IV}(T)
KZ14–58	Layered gabbro	Cpx	54.1	0.14	1.93	5.79	0.11	17.7	20.7	0.14	0.01	0.23	101	9	41	50	84.6	0.004	0.040
KZ14–57	Layered gabbro	Cpx	52.3	0.34	2.72	6.38	0.14	16.2	22.1	0.16	0.00	0.14	101	10	44	46	82.1	0.009	0.089
KZ14–56	Layered gabbro	Cpx	51.6	0.40	1.52	8.59	0.22	15.1	22.0	0.26	0.00	0.13	100	13	44	42	75.9	0.011	0.085
KZ14–55	Layered gabbro	Cpx	52.2	0.59	2.16	9.15	0.21	15.3	20.5	0.21	0.01	0.07	100	15	42	44	75.0	0.016	0.071
KZ14–54	Layered gabbro	Cpx	53.4	0.23	0.73	6.79	0.22	15.3	22.7	0.21	0.01	0.05	100	11	46	43	80.2	0.006	0.021
KZ14–53	Layered gabbro	Cpx	52.3	0.54	1.70	9.05	0.24	14.4	20.9	0.34	0.02	0.12	100	15	43	42	74.2	0.015	0.047
KZ14–52	Layered gabbro	Cpx	52.3	0.46	1.99	9.31	0.28	15.2	20.5	0.31	0.03	0.23	101	15	42	43	74.7	0.013	0.072
KZ14–46	Isotropic gabbro	Cpx	52.1	0.34	2.27	7.90	0.17	15.6	21.1	0.16	0.00	0.01	100	13	43	45	78.1	0.009	0.071
KZ14–45	Isotropic gabbro	Cpx	52.5	0.30	2.46	6.71	0.13	16.6	20.6	0.14	0.02	0.13	100	11	42	47	81.6	0.008	0.066
KZ14–41	Isotropic gabbro	Cpx	53.8	0.19	1.82	6.27	0.11	17.4	20.5	0.13	0.01	0.06	100	10	41	49	83.3	0.005	0.039
KZ14–44	Sheeted dike	Cpx	51.7	0.27	2.17	7.19	0.20	16.7	21.1	0.11	0.00	0.22	100	11	42	47	80.7	0.008	0.095
KZ14–50	Sheeted dike	Cpx	52.1	0.28	2.70	6.97	0.19	18.1	20.0	0.09	0.00	0.03	101	11	39	50	82.4	0.008	0.106

Note:$Fs=100\times Fe^{2+}/(Fe^{2+}+Mg^{2+}+Ca^{2+})$;$Wo=100\times Ca^{2+}/(Fe^{2+}+Mg^{2+}+Ca^{2+})$; $En=100\times Mg^{2+}/(Fe^{2+}+Mg^{2+}+Ca^{2+})$.
$Mg\# = 100\times Mg^{2+}/(Fe^{2+}+Mg^{2+})$.
Ti(M1) and Al^{IV}(T) are the molecular prop of cations, which is calculated on 6 O basis.

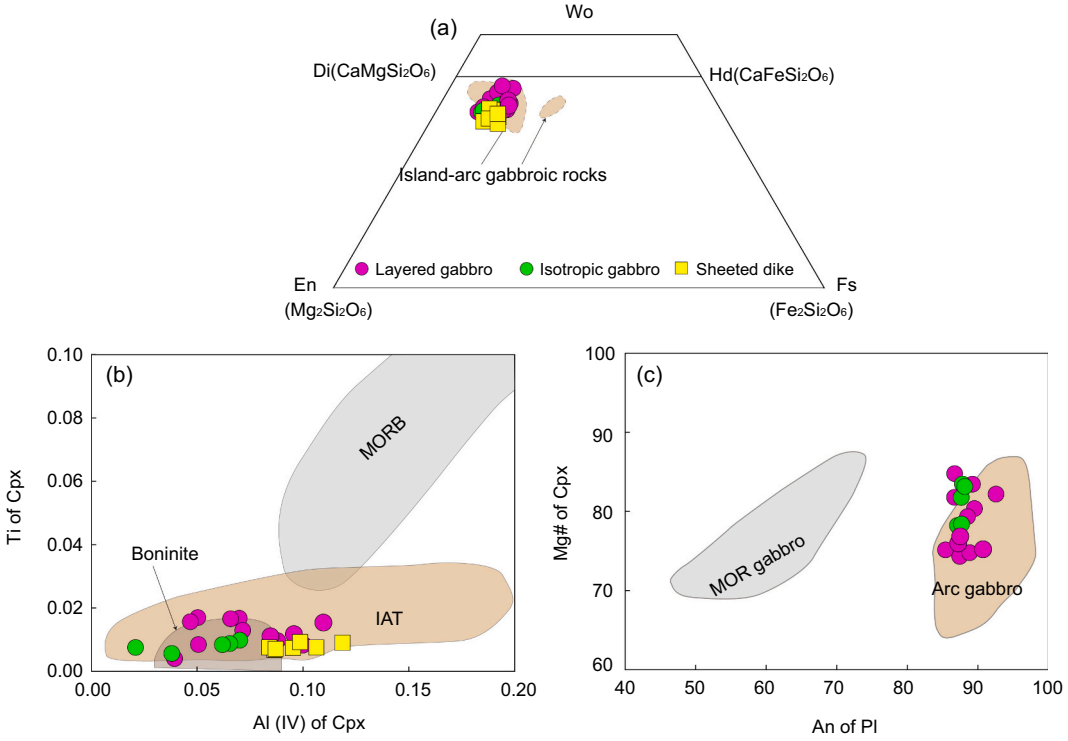

Fig. 4. Mineral composition diagrams for the Kızıldağ sheeted dikes and gabbros. (a) Clinopyroxene Wo-En-Fs diagram (after Burns (1985)), (b) Ti vs. Al (IV) of clinopyroxene (after Beccaluva et al. (1989)), (c) Mg# of clinopyroxene vs. An of plagioclase (after Burns (1985)).

(Li et al., 2015). Measured Pb isotopic ratios were corrected for instrumental mass fractionation of 1.2‰ per atomic mass unit by reference to repeated analyses of the NIST 981 Pb standard.

4. Results

4.1. Mineral compositions

Clinopyroxene grains in the sheeted dikes, layered gabbros, and isotropic gabbros have similar compositions (Table 1), plotting within the fields for island-arc gabbroic rocks (Fig. 4a). Clinopyroxene of the sheeted dikes has Mg# values of 77.2 to 82.4 and contains 0.25–0.34 wt % TiO_2 and 1.54–3.14 wt% Al_2O_3 (Table 1). Clinopyroxene of the layered gabbros has Mg# values of 74.2 to 84.6 and contains 0.14–0.60 wt% TiO_2 and 0.49–2.72 wt% Al_2O_3, whereas that in the isotropic gabbro has Mg# values of 78.1 to 83.3 and contains 0.19–0.34 wt% TiO_2 and 1.56–2.75 wt% Al_2O_3 (Table 1). On a plot of Ti and Al (IV), most of the clinopyroxene in the layered and isotropic gabbros falls in the field of boninite, whereas that of the sheeted dikes is within the field of IAT (Fig. 4b). Plagioclase of the layered and isotropic gabbros varies in composition from bytownite to anorthite (An_{79-93}), and plots in the field of arc gabbro (Fig. 4c). Although caution is warranted in using these discrimination diagrams based on mineral compositions, the results are consistent with those yielded by the whole-rock compositions.

4.2. Whole-rock major and trace element compositions

The sheeted dikes have Mg# values of 61.5 to 73.5 and contain 12.9–16.1 wt% Al_2O_3 (Table 2). They have La_N/Yb_N ratios of 0.33 to 0.62 and display LREE-depleted patterns similar to those of N-MORB, but have lower ∑REE concentrations, more similar to those of fore-arc basalt (FAB) (Li et al., 2019) (Fig. 5a). The sheeted dikes also exhibit similar patterns to FAB on a N-MORB-normalized, multi-element diagram (Fig. 5b).

The isotropic gabbros have Mg# values of 63.6 to 77.7 and contain 15.5 to 16.2 wt% Al_2O_3, similar to those of the sheeted dikes, whereas the layered gabbros have relatively higher Mg# values (70.4 to 83.9) but similar Al_2O_3 contents (13.7 to 16.7 wt%) (Table 2). Both the layered and isotropic gabbros have LREE-depleted patterns with La_N/Yb_N ratios of 0.19–0.53 and 0.39–0.64, respectively (Fig. 5c). The layered gabbros have REE concentrations ranging from 0.81 to 8.75 × chondrite, which are lower than those of the isotropic gabbros (from 1.79 to 16.06 × chondrite) (Table 2). Compared to the sheeted dikes, the isotropic and layered gabbros have relatively lower trace element concentrations and more scattered patterns (Fig. 5c, d), plotting in the fields of FAB and boninite (Fig. 5c, d).

The sheeted dikes have similar geochemical features to those of basalt and basaltic andesite on the plot of Nb/Y versus Zr/Ti (Fig. 6a), and plot in the fields of N-MORB and arc-related basalt (ARC) (Fig. 6b). They have Ti/V ratios between 10 and 20 on the plot of V versus Ti/1000 (Fig. 6c), consistent with values for island arc tholeiite (IAT) (Shervais, 1982). The sheeted dikes are displaced from the MORB-OIB array toward the oceanic arc field on the plot of Th/Yb versus Nb/Yb, consistent with the range for lavas of the Izu-Bonin-Mariana region (IBM) (Fig. 6d).

4.3. Whole-rock Pb isotope data

The sheeted dikes and gabbros have age-corrected $^{206}Pb/^{204}Pb_{(90\ Ma)}$ values ranging from 17.765 to 19.361, $^{207}Pb/^{204}Pb_{(90\ Ma)}$ from 15.570 to 15.665 and $^{208}Pb/^{204}Pb_{(90\ Ma)}$ from 37.812 to 39.269 (Table 3). They all have $^{207}Pb/^{204}Pb$ and $^{208}Pb/^{204}Pb$ ratios higher than those of MORB at a given $^{206}Pb/^{204}Pb$ ratio and are slightly displaced from the Northern Hemisphere Reference Line (NHRL; best-fit line through North Atlantic and Pacific MORB and ocean-island basalt, Hart, 1984) (Fig. 7). In the diagram of $^{206}Pb/^{204}Pb$ vs. $^{208}Pb/^{204}Pb$ (Fig. 7a), most samples span the fields between Indian Ocean MORB and modern marine sediments (or melts/fluids thereof).

Table 2
Whole-rock (wt%) and trace element (ppm) compositions of the gabbro and sheeted dike samples from the Kızıldağ ophiolite.

Sample	KZ15–06	KZ14–58	KZ14–57	KZ14–56	KZ14–55	KZ14–54	KZ14–53	KZ14–52	KZ14–46	KZ14–45	KZ14–42	KZ14–41	KZ15–04
Rock	Layered	gabbro							Isotropic	gabbro			
SiO_2	48.4	48.7	49.3	49.4	49.7	48.8	49.9	48.0	53.2	51.9	50.7	48.8	55.5
TiO_2	0.18	0.22	0.22	0.23	0.41	0.33	0.39	0.36	0.52	0.46	0.47	0.21	1.05
Al_2O_3	16.7	13.7	15.6	13.7	15.5	15.0	14.6	15.8	15.9	16.2	15.5	16.1	14.8
TFeO	3.64	5.09	6.06	7.10	6.16	6.53	6.52	7.40	7.90	7.30	7.46	5.44	10.3
MnO	0.09	0.12	0.13	0.15	0.11	0.13	0.13	0.13	0.17	0.14	0.13	0.12	0.21
MgO	10.6	12.1	10.5	11.7	9.64	9.94	9.37	9.79	7.66	8.35	10.0	10.5	5.20
CaO	16.4	15.1	14.8	13.7	13.2	15.0	15.5	13.0	8.26	7.59	8.40	11.6	5.04
Na_2O	1.08	1.29	0.75	0.94	1.61	1.24	1.31	1.59	2.77	3.87	2.23	2.45	4.05
K_2O	0.03	0.05	0.04	0.04	0.12	0.05	0.04	0.08	0.53	0.45	0.65	0.14	0.79
P_2O_5	0.01	0.01	0.01	0.01	0.02	0.01	0.01	0.01	0.04	0.03	0.03	0.01	0.07
LOI	2.36	2.60	1.22	1.18	2.26	1.56	1.10	2.38	1.98	2.96	3.94	3.80	1.78
Total	99.9	98.9	98.6	98.1	98.7	98.5	98.8	98.6	98.9	99.2	99.6	99.3	100
La	0.19	0.26	0.39	0.26	0.56	0.50	1.00	0.41	1.43	1.21	0.87	0.47	2.28
Ce	0.53	0.70	0.88	0.72	1.59	1.37	2.06	1.17	3.24	2.80	2.04	1.10	5.03
Pr	0.11	0.14	0.16	0.14	0.33	0.27	0.42	0.23	0.55	0.50	0.38	0.19	0.89
Nd	0.67	0.93	0.96	0.96	2.09	1.74	2.41	1.52	3.08	2.87	2.26	1.11	4.97
Sm	0.34	0.45	0.42	0.47	0.89	0.78	0.98	0.67	1.17	1.06	0.94	0.44	1.79
Eu	0.17	0.20	0.20	0.22	0.41	0.37	0.42	0.34	0.50	0.44	0.40	0.22	0.68
Gd	0.59	0.79	0.72	0.85	1.46	1.23	1.46	1.09	1.74	1.61	1.51	0.70	2.71
Tb	0.13	0.16	0.15	0.18	0.29	0.26	0.31	0.23	0.35	0.34	0.31	0.15	0.55
Dy	0.94	1.21	1.16	1.36	2.02	1.85	2.15	1.66	2.53	2.367	2.32	1.08	3.85
Ho	0.21	0.27	0.27	0.31	0.45	0.41	0.48	0.38	0.56	0.55	0.52	0.24	0.88
Er	0.59	0.75	0.77	0.90	1.28	1.15	1.35	1.08	1.62	1.56	1.48	0.69	2.49
Tm	0.09	0.11	0.12	0.14	0.20	0.17	0.20	0.16	0.24	0.24	0.23	0.11	0.37
Yb	0.55	0.71	0.76	0.90	1.23	1.09	1.27	1.05	1.56	1.57	1.49	0.69	2.42
Rb	0.51	0.18	0.27	0.20	0.48	0.17	0.18	0.28	1.95	2.06	3.00	1.12	2.91
Sr	63.20	63.09	28.32	35.9	114.08	80.18	71.38	97.08	166.19	79.50	90.11	110.42	235.08
Ba	7.76	2.71	3.75	3.42	3.04	4.75	7.64	4.36	24.34	26.34	15.36	5.60	44.38
Th	0.03	0.03	0.08	0.04	0.07	0.05	0.22	0.04	0.19	0.19	0.12	0.07	0.35
U	0.01	0.01	0.01	0.01	0.02	0.02	0.02	0.01	0.08	0.07	0.04	0.03	0.13
Pb	0.14	b.d.	0.04	b.d.	b.d.	b.d.	0.69	b.d.	0.43	b.d.	0.02	b.d.	0.22
Cs	0.01	0.01	0.01	0.01	0.01	0.01	0.01	0.01	0.01	0.01	0.01	0.01	0.02
Lu	0.09	0.11	0.12	0.14	0.19	0.16	0.20	0.16	0.25	0.24	0.24	0.11	0.38
Hf	0.17	0.18	0.20	0.22	0.49	0.35	0.39	0.29	0.86	0.85	0.58	0.24	1.38
Nb	0.11	0.09	0.13	0.12	0.28	0.19	0.19	0.15	1.07	1.06	0.57	0.23	1.93
Ta	0.01	0.01	0.01	0.01	0.02	0.02	0.02	0.01	0.07	0.08	0.04	0.02	0.14
Zr	4.67	4.44	5.08	5.34	14.01	9.48	10.36	7.46	25.27	25.22	15.73	6.37	40.88
Y	4.68	6.77	6.65	7.76	11.60	10.22	12.00	9.29	14.94	14.31	13.79	6.06	21.46

KZ14–44	KZ14–51	KZ14–50	KZ14–49	KZ14–48	KZ14–47	KZ15–05	KZ15–01
Sheeted dike							
51.0	50.7	49.6	51.5	52.9	49.5	51.7	52.0
0.50	0.63	0.65	0.68	0.71	0.59	0.75	0.61
12.9	15.4	15.8	15.2	15.3	15.4	16.1	15.2
8.24	8.08	8.79	8.19	7.95	7.74	8.58	7.42
0.14	0.16	0.14	0.14	0.12	0.14	0.12	0.13
12.7	9.09	9.32	9.15	7.05	8.50	8.33	7.28
6.27	7.06	5.86	6.25	6.47	8.23	7.02	7.37
2.07	2.64	3.60	2.70	5.23	3.69	3.20	4.76
0.54	0.53	0.25	0.53	0.28	0.22	0.55	0.29
0.03	0.04	0.04	0.05	0.06	0.04	0.05	0.05
4.92	5.00	4.84	4.74	3.52	4.76	3.14	4.26
99.3	99.3	98.9	99.1	99.6	98.8	101	100
1.38	1.62	0.94	1.24	1.78	0.84	1.85	1.19
2.93	3.64	2.31	3.41	4.76	2.17	4.29	3.18
0.48	0.61	0.44	0.66	0.92	0.43	0.74	0.60
2.76	3.47	2.74	3.68	5.13	2.66	4.26	3.63
1.08	1.31	1.20	1.45	1.95	1.14	1.57	1.38
0.42	0.51	0.49	0.57	0.76	0.47	0.58	0.47
1.60	1.98	1.85	2.06	2.67	1.80	2.31	2.06
0.33	0.40	0.38	0.41	0.53	0.38	0.47	0.42
2.45	2.91	2.82	2.93	3.68	2.69	3.27	2.86
0.54	0.64	0.63	0.66	0.81	0.59	0.76	0.64
1.62	1.85	1.82	1.92	2.33	1.74	2.12	1.84
0.25	0.28	0.28	0.31	0.37	0.27	0.32	0.27
1.68	1.84	1.81	2.01	2.37	1.73	2.04	1.77
1.39	2.30	1.16	1.32	1.60	1.21	1.94	1.42
145.48	89.10	92.74	89.65	91.59	185.98	140.31	212.58
17.97	30.69	19.61	30.21	10.73	7.659	31.82	10.52
0.23	0.29	0.17	0.12	0.15	0.13	0.40	0.21
0.08	0.08	0.06	0.06	0.09	0.05	0.12	0.08

(*continued on next page*)

Table 2 (*continued*)

KZ14–44	KZ14–51	KZ14–50	KZ14–49	KZ14–48	KZ14–47	KZ15–05	KZ15–01
Sheeted dike							
0.16	b.d.	b.d.	0.62	0.61	b.d.	0.13	0.18
0.01	0.02	0.01	0.25	0.25	0.01	0.01	0.02
0.27	0.29	0.29	0.31	0.37	0.27	0.31	0.28
0.74	0.90	0.88	1.03	1.34	0.78	1.23	1.01
1.12	1.17	0.90	1.54	1.64	0.78	1.48	0.98
0.08	0.09	0.07	0.12	0.12	0.06	0.12	0.08
20.90	26.55	22.96	33.20	42.18	20.88	37.45	29.26
14.43	17.16	15.52	17.23	21.33	15.67	17.33	15.76

Note: b.d.: below detection limit.

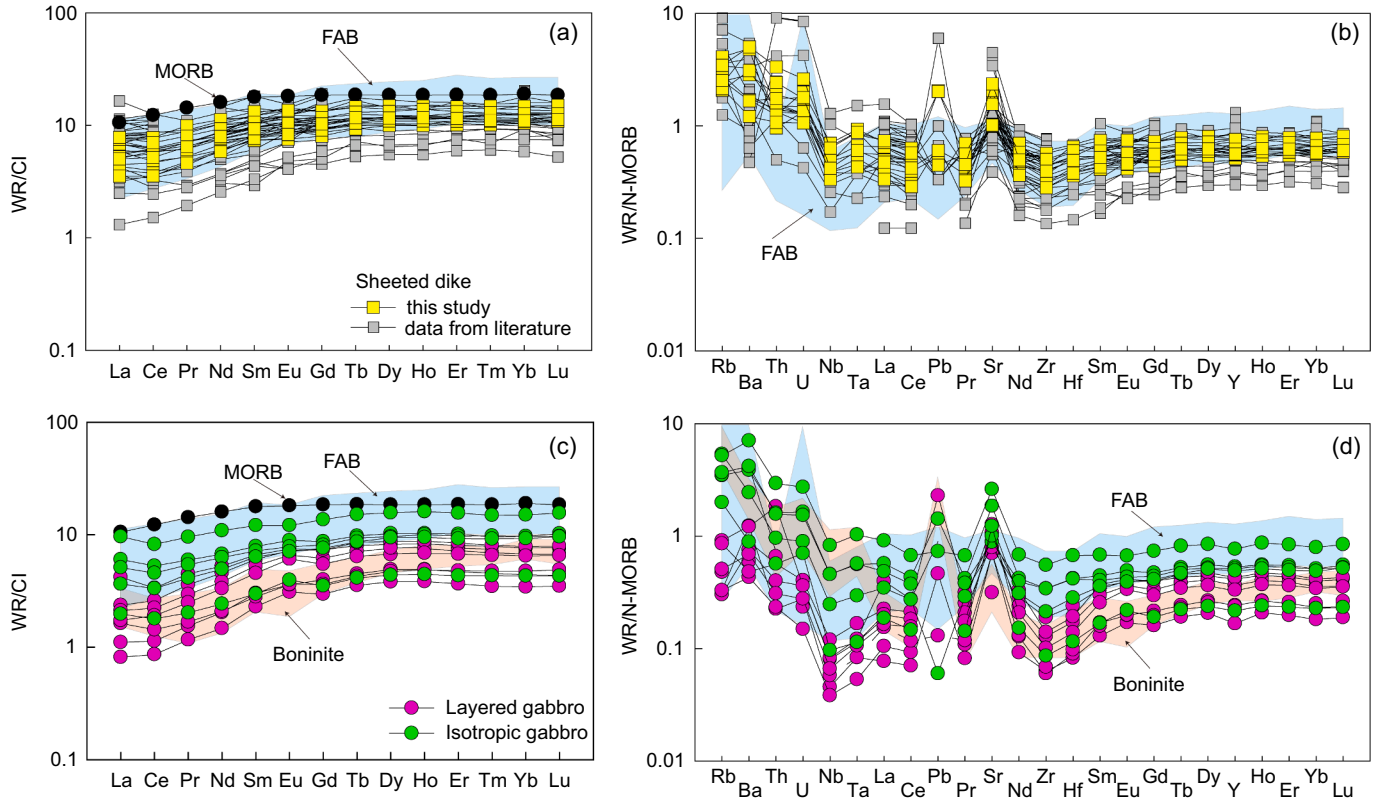

Fig. 5. (a, c) Chondrite-normalized REE (b, d) N-MORB-normalized incompatible trace element patterns for the sheeted dikes and gabbros of the Kızıldağ ophiolite (normalization values from Sun and McDonough, 1989). Forearc basalt field is after Shervais et al. (2019), and boninite field is after Woelki et al. (2018). Abbreviations: WR, Whole rock; FAB, forearc basalt.

5. Discussion

5.1. Effect of alteration

The gabbros and sheeted dikes of the Kızıldağ ophiolite have <5 wt% loss on ignition (LOI) and show only minor alteration of clinopyroxene to actinolite. We used two well-known alteration indices of whole-rock major element compositions, i.e., Ishikawa alteration index (AI), and the chlorite-carbonate-pyrite index (CCPI), to quantify the alteration degrees of the rocks (Mathieu, 2018). The AI and CCPI values of our samples are ~36 to 61 and ~45 to 71, respectively (Table 2), and all fall into the least altered fields (AI = ~20–65 and CCPI = ~40–85) of felsic-mafic rocks (Gifkins et al., 2005). We therefore consider that our samples underwent only weak alteration and that the major element compositions of the rocks have been very little modified. This interpretation is supported by positive correlations of Zr with HFSE (e.g., Nb, V and Y) and REE (e.g., La, Sm and Yb) (Fig. S1) in the analyzed rock. Because Zr is generally considered to be immobile during alteration (Gibson et al., 1982), its positive correlations with these trace elements indicate little, if any, modification by hydrothermal alteration (e.g., Gibson et al., 1982; Qiu et al., 2011). Likewise, neither the trace elements nor the Pb isotopes show correlations with LOI (Fig. S1), also pointing to only minor alteration.

5.2. Nature of the mantle source

It is widely accepted that the lavas and dikes with high MgO contents (> 8.5 wt%) could represent their parental magmas (e.g., Elitok, 2012; Hawkins et al., 1984; Lee et al., 2009; Woelki et al., 2018). Here, the sheeted dikes from the Kızıldağ ophiolite usually have a sharp boundary and display chilled margins, and hence the most MgO-rich samples (> 8.5 wt% and even up to 12.7 wt%) undoubtedly contain useful information about the early magmas from which they were formed. The sheeted dikes have trace element concentrations lower than those of MORB, but similar to those of FAB (Fig. 5a, b), indicating derivation from a relatively depleted mantle source in a forearc setting (Pearce and

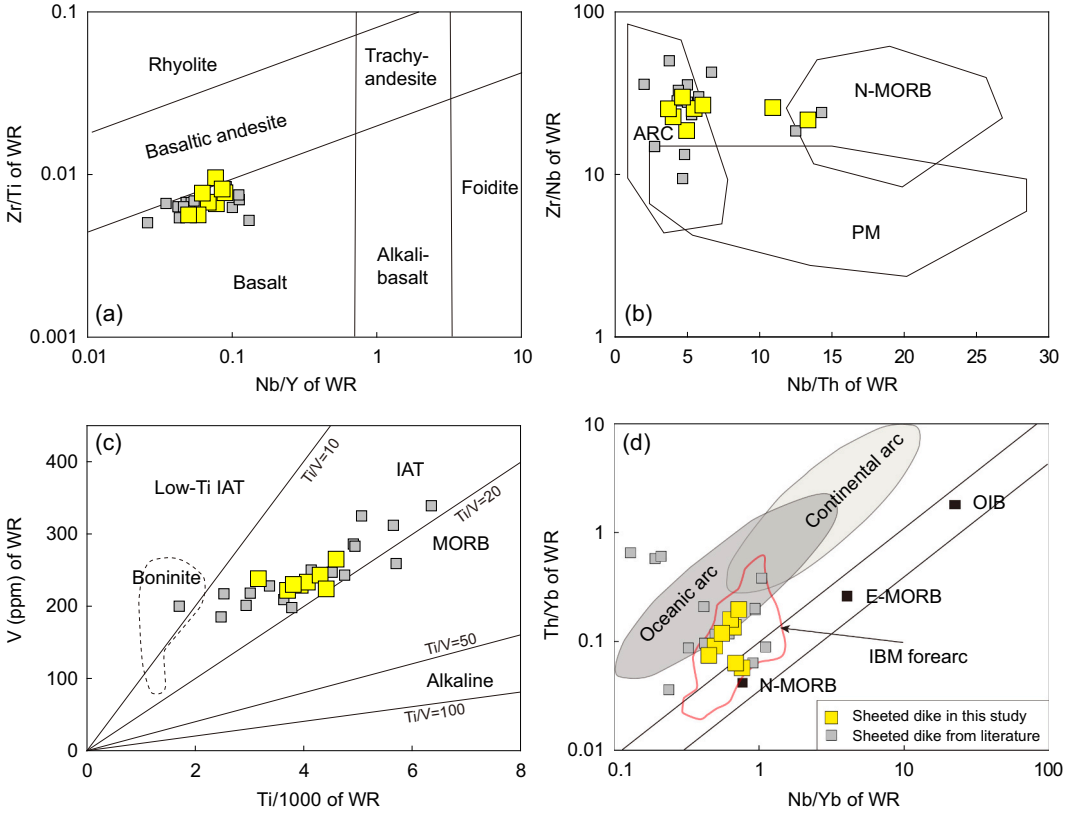

Fig. 6. Trace element diagrams for sheeted dikes of the Kızıldağ sheeted dikes, (a) Zr/Ti vs. Nb/Y, (b) Zr/Nb vs. Nb/Th, (c) V vs. Ti/1000 (d) Th/Yb vs. Nb/Yb. (a) modified after Pearce (1996), (b) modified after Condie (2005), (c) and (d) modified after Pearce (2014). The field of IBM forearc is after Lian et al. (2017). Abbreviations: MORB: mid-ocean ridge basalt; IBM, Izu-Bonin-Mariana; IAT, island arc tholeiite; N-MORB, normal MORB; E-MORB, enriched MORB; OIB, ocean island basalt; PM, primary mantle; ARC, arc-related basalt.

Table 3
Pb isotopes of the gabbro and sheeted dike samples from the Kızıldağ ophiolite.

Sample	Rock type	$^{206}Pb/^{204}Pb$	2se	$^{207}Pb/^{204}Pb$	2se	$^{208}Pb/^{204}Pb$	2se	$(^{206}Pb/^{204}Pb)_{90Ma}$	$(^{207}Pb/^{204}Pb)_{90Ma}$	$(^{208}Pb/^{204}Pb)_{90Ma}$
KZ15–06	Layered gabbro	18.652	0.005	15.621	0.005	38.744	0.012	18.559	15.617	38.682
KZ14–57	Layered gabbro	18.356	0.004	15.591	0.003	38.457	0.007	18.075	15.577	37.812
KZ14–53	Layered gabbro	18.739	0.008	15.585	0.007	38.722	0.017	18.715	15.584	38.619
KZ14–43	Isotropic gabbro	19.143	0.003	15.605	0.003	39.261	0.009	18.940	15.595	39.048
KZ15–04	Isotropic gabbro	18.348	0.004	15.613	0.003	38.581	0.008	17.765	15.585	38.068
KZ14–44	Sheeted dike	19.113	0.002	15.593	0.002	39.064	0.004	18.634	15.570	38.612
KZ14–49	Sheeted dike	18.728	0.017	15.670	0.015	38.990	0.041	18.626	15.665	38.931
KZ14–48	Sheeted dike	19.515	0.004	15.631	0.003	39.348	0.007	19.361	15.623	39.269
KZ15–05	Sheeted dike	19.550	0.005	15.648	0.004	39.548	0.013	18.635	15.604	38.594

Parkinson, 1993; Shervais et al., 2019). High Th/Yb ratios of these samples (Fig. 6d) are consistent with some contribution of slab-derived components to the parental magmas (Pearce, 2008), consistent with the scattered Pb isotopic compositions of the samples (Fig. 7), which indicate addition of variable quantities of slab-derived components (Grove et al., 2002). Thus, we suggest that the sheeted dikes of the Kızıldağ ophiolite may have the compositions close to their FAB-like parental magmas, which were likely generated by partial melting of a depleted mantle source metasomatized by slab-derived components.

The gabbros have lower REE and trace element concentrations than the sheeted dikes (Fig. 5), suggesting that they may be related to low fractions of trapped liquid in the cumulates, because the incompatible trace elements would preferentially partition into the extracted melts during fractionation. Both the gabbros and sheeted dikes have relatively restricted Sm/Yb and La/Sm ratios (Fig. 8a), but the gabbros have lower La contents and La/Sm ratios than the sheeted dikes (Fig. 8b). These observations suggest that the parental magmas of the gabbros may have been more depleted than those of the sheeted dikes. This interpretation is also supported by the MORB-normalized trace element diagrams, in which the isotropic and layered gabbros straddle the boundary between FAB and boninites (Fig. 5c, d). In addition, the clinopyroxene grains of the gabbros have compositions similar to those of boninites (Fig. 4b). We therefore suggest that the parental magmas of the gabbros were most likely boninitic.

5.3. *P-T-fO_2 conditions of mantle melting*

In order to prescribe a general limit to the following forward models for partial melting processes, we adopted the major element compositions of the sheeted dikes to estimate the temperatures (T) and pressures (P) under which partial melting of the Kızıldağ mantle may have occurred. We also examined the redox states of the mantle using the V and Yb concentrations of these rocks. It has been widely accepted that the compatibility of V is strongly influenced by oxygen fugacity; V

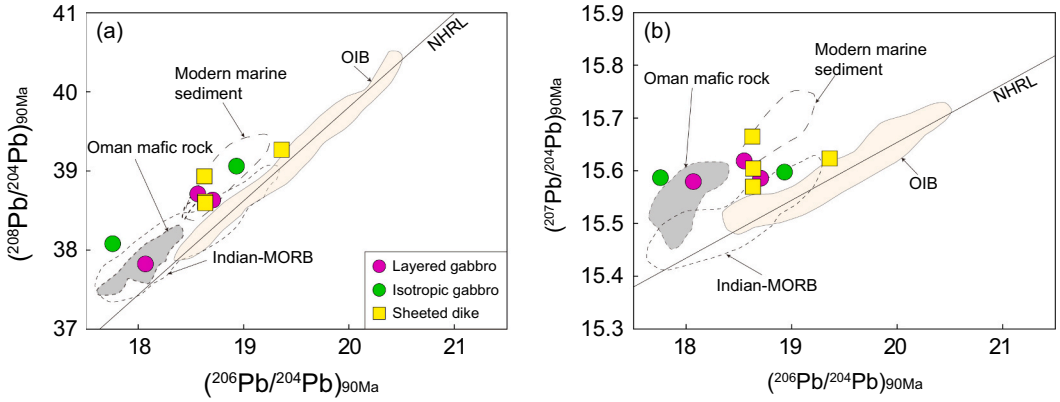

Fig. 7. Pb isotope plots for the Kızıldağ sheeted dikes and gabbros. (a) $^{208}Pb/^{204}Pb$, (b) $^{207}Pb/^{204}Pb$ ratios versus $^{206}Pb/^{204}Pb$ ratios. All points are recalculated at 90 Ma. Data sources for the OIBs, MORB, modern marine sediments and Oman mafic rock data are from Godard et al. (2006) and references therein. Abbreviations: NHRL, Northern Hemisphere Reference Line.

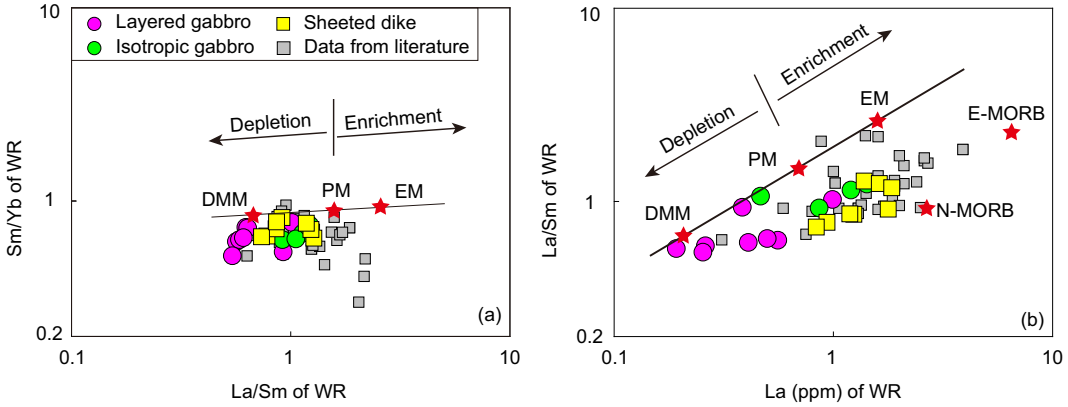

Fig. 8. Plots of various trace element ratios for the Kızıldağ ophiolite. (a) Sm/Yb vs. La/Sm, (b) La/Sm vs. La. The gray squares represent the sheeted dike data from the literature (Bagci et al., 2008; Dilek and Furnes, 2009; Dilek and Thy, 2009). Depleted MORB mantle (DMM) and primitive mantle (PM) are from Sun and McDonough (1989), and enriched mantle (EM) is from Aldanmaz et al. (2000).

behaves as a moderately incompatible element in low oxygen fugacity but becomes highly incompatible under high oxygen fugacity (Pearce and Parkinson, 1993). According to the concentrations of V and Yb, the oxygen fugacity of the dikes is calculated to be around ΔFMQ (Fig. 9a). To the extent that these MgO-rich dikes have a close affinity to their parental magmas, this estimation maybe an approximation of the oxygen fugacity of mantle source. Our calculated value is higher than that of MORB mantle (ΔFMQ−1), but lower than that of IAT mantle (ΔFMQ+1) (Pearce and Parkinson, 1993). Moreover, this result is comparable with the mantle oxygen fugacity of the volcanic rocks in the IBM arc-basin system.

The temperatures and pressures at which the melt was generated and extracted from the mantle wedge can be constrained using the silica activity thermobarometer proposed by Lee et al. (2009) (Fig. 9b-d). This SiO_2-based thermobarometer is less sensitive to variations in mantle compositions because SiO_2 is buffered by the mineralogy of the system (Lee et al., 2009). Firstly, the compositions of these MgO-rich sheeted dikes were corrected for olivine fractionation up to olivine Fo number of 90. Then the Fe^{3+}/Fe values of melts were assumed to be 0.12 based on the ΔFMQ setting of the mantle source (Jayasuriya et al., 2004; Lee et al., 2009). Here, the estimated P and T values of these parental magmas can be taken to represent the weighted average pressure and temperature conditions of melting events that occurred in the mantle wedge. Given that mafic arc magmas usually contain 2–6 wt% H_2O with an average of 3.9 wt% (Plank et al., 2013), the H_2O contents of these possible parental magmas were set to be 0 wt% (Fig. 9b), 3 wt% (Fig. 9c) and 6 wt% (Fig. 9d) for modelling purposes. The results show that the ranges of the equilibrium T-P conditions for partial melting of the mantle mainly vary from 1249 to 1383 °C and from 0.27 to 1.20 GPa for anhydrous melt (Fig. 9b), 1200–1319 °C and 0.52–1.42 GPa for the melt with 3 wt% H_2O (Fig. 9c), and 1108–1262 °C and 0.77–1.38 GPa for melt with 6 wt% H_2O (Fig. 9d). The addition of water into a mantle source can depress the peridotite solidus and induce flux-melting of the mantle wedge at higher pressures and lower temperatures (e.g., Grove et al., 2012). The estimated P-T values also coincide with those of primary magmas in continental arcs that were last equilibrated with their source at ~1 GPa and 1100–1300 °C (Grove et al., 2012; Yao et al., 2018). Given that the obtained pressures are about 1 GPa regardless of water contents, the parental magmas of these sheeted dikes were likely generated at shallow depth (35–40 km), well above the subducting slab (Fig. 9b-d).

To sum up, we adopted the compositions of MgO-rich sheeted dikes to estimate the P-T-fO_2 conditions of mantle melting events for the Kızıldağ ophiolite. These estimates suggest that the parental magmas may have been generated at a relatively shallow depth (~1 GPa or 35–40 km), in a moderate thermal state (~1200–1300 °C) and an oxygen fugacity condition (~ΔFMQ), all of which are also comparable to the equilibrium thermodynamic conditions of the IBM basalt and boninite.

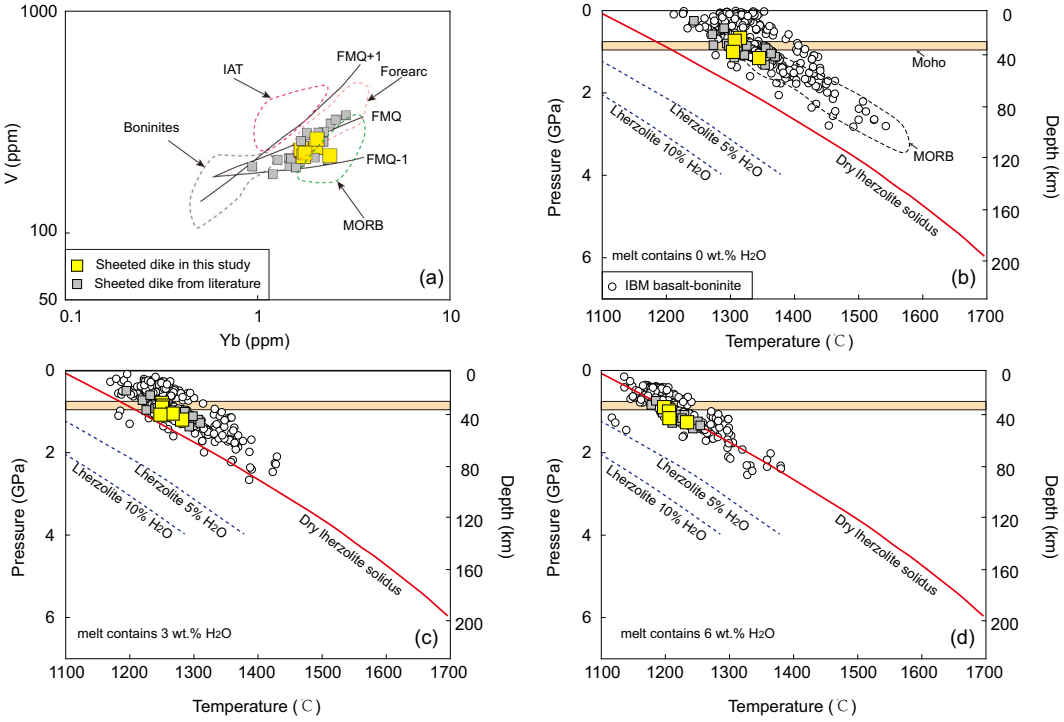

Fig. 9. (a) Plot of V vs. Yb for the Kızıldağ sheeted dikes (after Pearce and Parkinson (1993)). (b-d) The estimated temperature and pressure of the melt generation for the Kızıldağ sheeted dikes (only the rocks with MgO > 8.5 wt% were used adopted here). The lherzolite solidus at varying water contents is taken from Katz et al. (2003). Data of MORB and IBM basalt-boninite are compiled from the GEOROC database.

5.4. *Modelling of polybaric continuous melting and isobaric flux-melting*

With the P-T-fO_2 parameters calculated above, we simulated polybaric continuous melting of depleted MORB mantle (DMM) and flux-melting of a mantle wedge to examine the complicated partial melting processes of the Kızıldağ ophiolite. Polybaric continuous melting associated with convection-induced pressure release, which is similar to the partial melting models at mid-ocean ridges, has been proposed to operate in subduction zones, particularly during early slab rollback (e.g., Behn et al., 2011; Cooder et al., 2002; Kohut et al., 2006; Lee et al., 2009; Yao et al., 2018). On the other hand, the presence of H_2O depresses the peridotite solidus in subduction zones, and an influx of slab-derived hydrous melts/fluids induces further flux-melting in the mantle wedge (e.g., Grove et al., 2002, 2012). In this scenario, polybaric continuous melting and flux-melting can be considered as two end-member models, but partial melting of mantle wedges in arc systems likely occurs along a continuous spectrum between them. The relative contributions of these end-members to the final magmas may depend on the physical parameters of each subduction zone, such as convergence rate and angle, slab age, and slab dip (e.g., Lee et al., 2009; Van Keken, 2003). Because these physical parameters are difficult to determine for the Kızıldağ ophiolite, the two end-member, partial melting models are simultaneously adopted here to obtain a first-order understanding of the magma generation in subduction zones, which may contribute to better quantitative models. Therefore, in the following sections, we combine the estimated P-T-fO_2 conditions for mantle melting and model the compositional evolution of resultant melts produced by polybaric continuous melting and isobaric flux-melting of the mantle source using the latest version of alphaMELTS (Smith and Asimow, 2005).

For the models of polybaric continuous melting, we used the well-

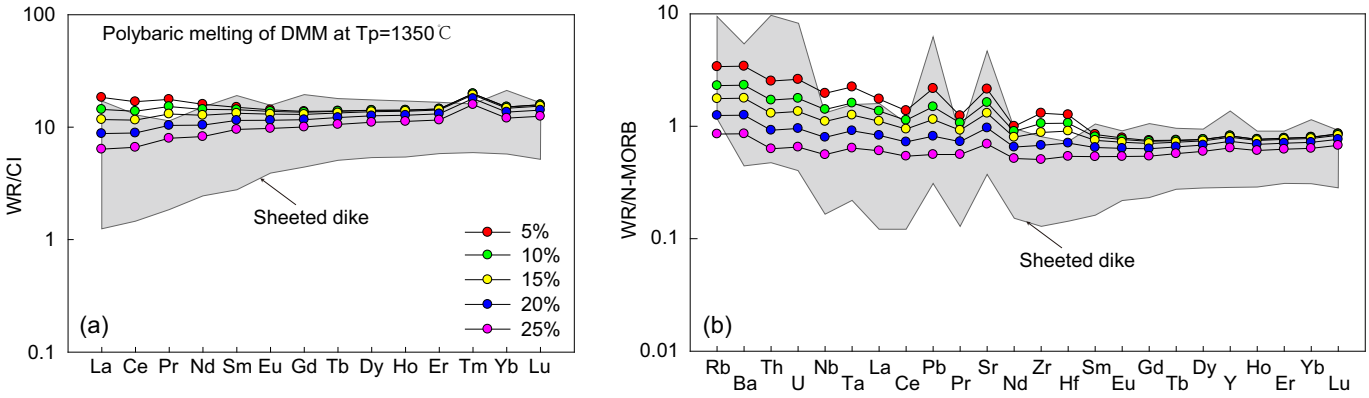

Fig. 10. (a, b) Polybaric continuous melting model for the Kızıldağ sheeted dikes is shown on the chondrite-normalized REE and N-MORB-normalized multi-element diagrams, respectively. Normalization values are from Sun and McDonough (1989). The curves are magmatic compositions after 5%, 10%, 15%, 20% and 25% melting of DMM (depleted MORB mantle), respectively.

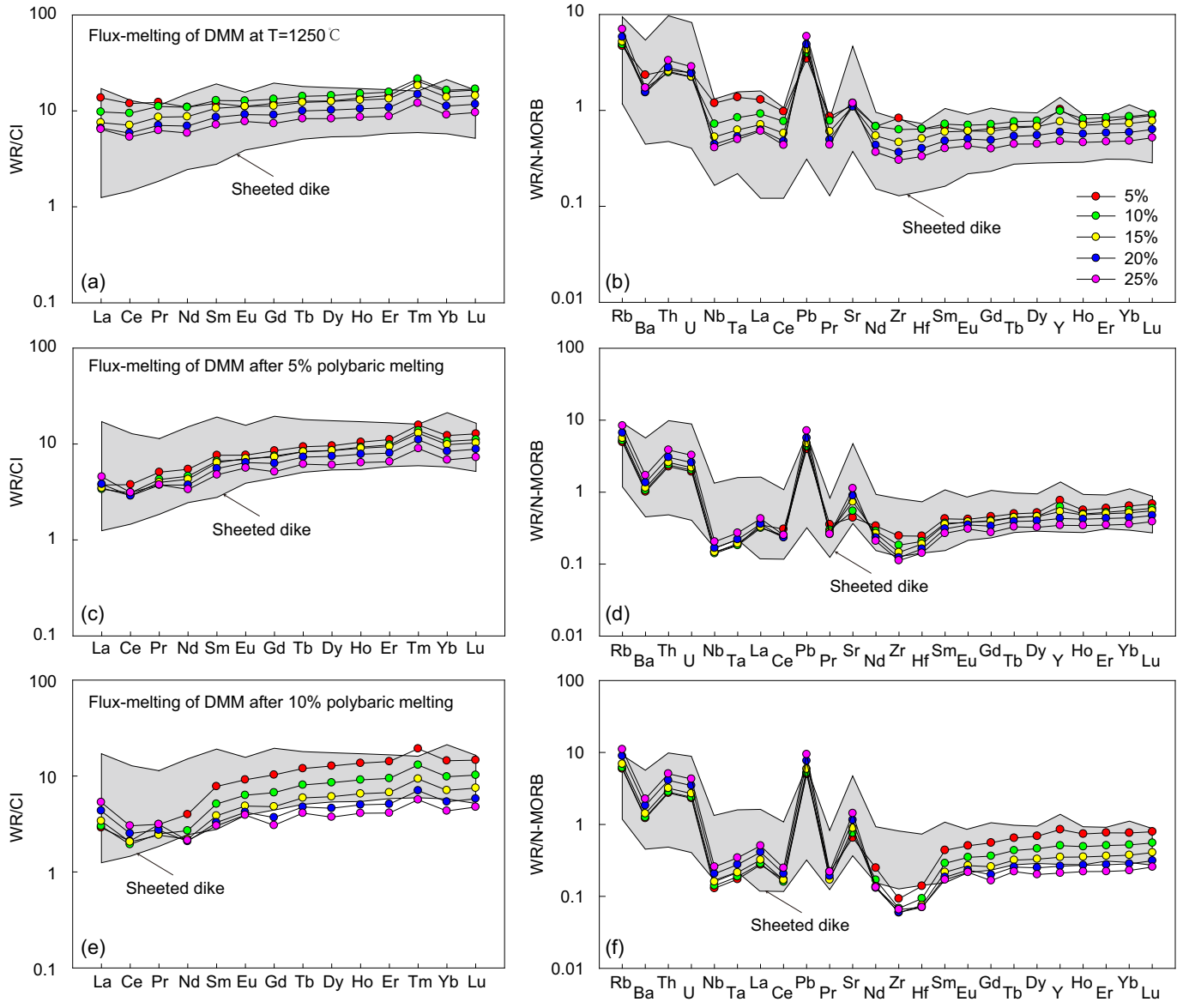

Fig. 11. Isobaric flux-melting models for the Kızıldağ sheeted dikes are shown on the chondrite-normalized REE (a, c, e) and N-MORB-normalized multi-element (b, d, f) diagrams. Normalization values are from Sun and McDonough (1989).

accepted composition of DMM (Workman and Hart, 2005) with a mantle potential temperature of 1350 °C as the starting mantle material (Yao et al., 2018). The approach used for computing this melting model has been described in detail by Asimow et al. (2001). Decompression of the DMM was simulated from the solidus to the surface in 10 MPa steps, and the thermodynamic equilibrium between the restite and melt was modelled in each increment. Once the melt fraction exceeds ~1 vol%, the extra part in each increment should be extracted, and the composition and entropy of the residual system used as a reference for the next increment. Finally, the increments of extracted melts were integrated as the pooled magmatic output of mantle melting (the operating instruction to conduct this decompression melting model via AlphaMELTS is here, http://magmasource.caltech.edu/alphamelts/1/exercises-for-melts.htm). In this modelling, we adopted the default partition coefficients from AlphaMELTS, in which the variable REE partition coefficients of clinopyroxene/melt and plagioclase/melt were estimated based on the classical lattice strain theory (Blundy and Wood, 1994; Wood and Blundy, 1997). The constant partition coefficients for the remaining elements and melt-solid pairs were taken from earlier studies (McKenzie and O'Nions, 1991, 1995). The modelled REE and trace element patterns of pooled melts at different melting degrees (5–25%) overlap the compositions of some sheeted dikes of the Kızıldağ ophiolite, but only occupy the ranges at high concentrations (Fig. 10a, b). Hence, most sheeted dike samples cannot be interpreted simply as the products of such a melting model, especially for those samples with depleted LREE and HFSE (Fig. 10b). Therefore, polybaric melting of the DMM appears to have been active, but it alone cannot explain the range of trace element patterns of the sheeted dikes of the Kızıldağ ophiolite.

We also conducted the isobaric flux-melting model, in which the progressive addition of small amounts of slab-derived melts/fluids and the removal of generated melts occurs simultaneously at constant P-T condition close to the anhydrous solidus of the mantle wedge peridotite (Yao et al., 2018). A constant pressure for the flux-melting model was assumed to be 1.0 GPa, and the corresponding temperature was set at 1250 °C for simplification, which also matches our estimates from the previous section. Because mantle wedges above subduction zones have likely experienced multiple melting events and/or metasomatisms, their compositions are poorly understood. To circumvent this problem, the

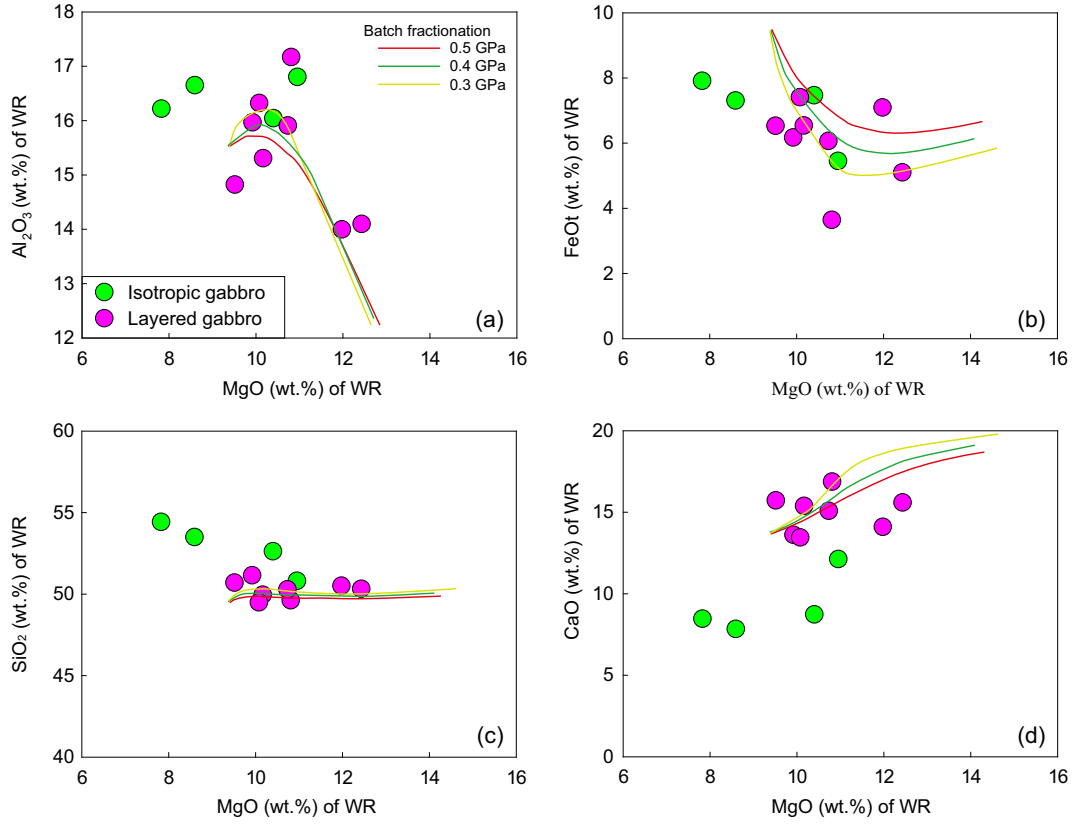

Fig. 12. Plots of Al_2O_3 (a), FeOt (b), SiO_2 (c) and CaO (d) vs. MgO for the whole-rock compositions from the Kızıldağ layered gabbros and isotropic gabbros. Color lines represent the compositional evolutions of the cumulate during the batch fractionation of a boninitic melt (sample K-25A from Bagci et al., 2008) at different pressure conditions (0.3, 0.4 and 0.5 GPa).

DMM composition was set to approximate the source of arc magmas in order to compare the two end-member melting models. Considering that the mantle wedges generally have undergone variable degrees of depletion due to preceding melting events, the restites resulting after 5% and 10% melt extraction from polybaric continuous melting of DMM were also adopted as the possible initial source compositions, and termed as 5%-depleted DMM and 10%-depleted DMM. This assumption of source composition is not perfect, but seems to be acceptable (Yao et al., 2018). Keeping these plausible scenarios in mind, our modelling could provide a first-order understanding of the flux-melting process, which has yet to be modelled quantitatively. For isobaric flux-melting, 0.02 wt% of the slab-derived melts/fluids were added to the system at each increment, and the portion of melt exceeding 1 vol% in each increment was extracted and pooled to form the final magmatic output. The compositions of the slab-derived melts/fluids were obtained from the modelled results for the subduction system in SW Japan, where the trace elements of the slab-derived melts/fluids are proposed to have been released from altered oceanic crust (60–80%) and sediment (7–16%) (Kimura, 2017). With the assumed source compositions varying from DMM (Fig. 11a, b), to 5%-depleted DMM (Fig. 11c, d) and 10%-depleted DMM (Fig. 11e, f) in the isobaric flux-melting model, the final melts record gradually decreasing REE and HFSE, and increasing LILE (Fig. 11). Here, the modelled REE and trace elements patterns of the integrated melts are in a good agreement with the range of the sheeted dikes of the Kızıldağ ophiolite (Fig. 11), indicating that highly variable source compositions and partial melting mechanisms in the complex subduction zones may both be crucial factors controlling the final melting products. On the other hand, subsequent crystallization of these magmas prior to emplacement cannot account for the variabilities of trace elements that vary by more than one order of magnitude, which would require an extremely large degree of fractionation. For example, an incompatible element would require ~90% crystallization to drive the increase of its content from 1 to 10. The textures and compositions of the Kızıldağ sheeted dikes do not show any obvious evidence of fractionation, hence the variabilities of their trace elements mostly reflect the variety of partial melting events. The observed variabilities cannot be attributed to partial melting of a fixed source via only one melting mechanism (either polybaric continuous melting or flux-melting).

To sum up, the modelling results suggest that the sheeted dikes of the Kızıldağ ophiolite may be the integrated products of <10% polybaric continuous melting of a DMM-like source and < 25% flux-melting of the mantle wedge. The complex melting processes may explain the large compositional variations of the sheeted dikes from FAB to IAT-like. Hence, we infer that these sheeted dikes may have formed from magmas that were generated during subduction initiation, where decompression melting and flux-melting processes imposed comprehensive influences on the final melting products.

5.5. *Parental magmas of the layered and isotropic gabbro*

We also carried out a series of models to simulate the formation of the gabbros by crystal fractionation. In order to avoid introducing

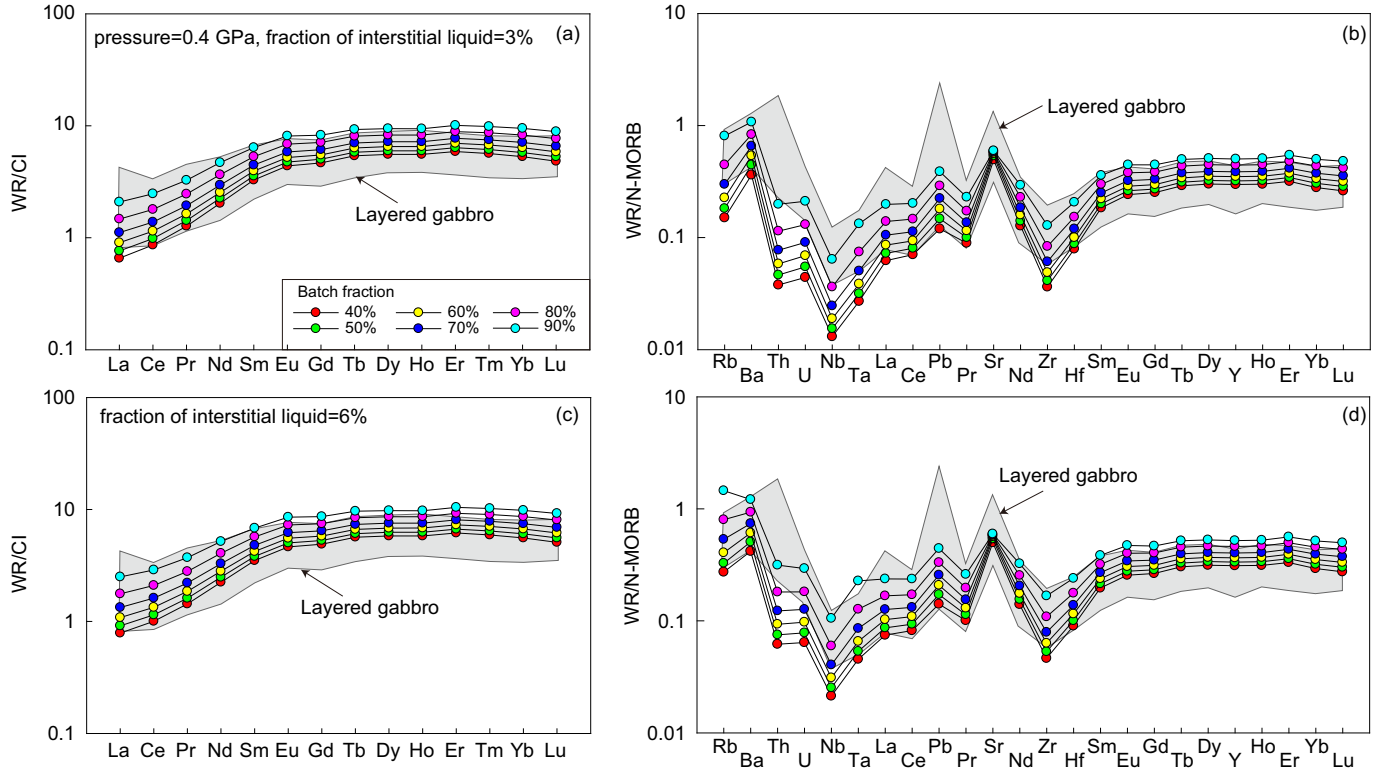

Fig. 13. Batch fractionation models for the Kızıldağ layered gabbros are shown on the chondrite-normalized REE (a, c) and N-MORB-normalized multi-element (b, d) diagrams. Normalization values are from Sun and McDonough (1989). The curves represent the compositions of cumulates through 40%, 50%, 60%, 70%, 80% and 90% crystallization, with different fractions of interstitial liquid (3 wt% and 6 wt%).

uncertainty into the modelling results, we searched for a plausible parental magma from the boninitic-type sheeted dikes sited in the same region based on the geochemical features of gabbros (Figs. 4, 5). After comparing all the data of the sheeted dikes from the previous studies (e.g., Bagci et al., 2005, 2008; Dilek and Furnes, 2009; Dilek and Thy, 2009) and this work, we adopted a fresh boninitic-type dike (K-25A) from Bagci et al. (2008) that has the lowest LOI (0.17 wt%), moderate MgO (~10 wt%) and Mg# (~64.3) as a likely reference point to model magma evolution of the gabbros. This choice generated a non-unique, but generally satisfactory, match to the available data and therefore is considered a plausible parental magma for the gabbros. Based on the clinopyroxene thermobarometric method proposed by Putirka (2008), we estimated the crystallization temperatures and pressures for the layered and isotropic gabbros. The layered gabbros yielded equilibrium temperatures and pressures of ~1176–1186 °C and 0.39–0.55 GPa, respectively, which are similar to those for the isotropic gabbros (~1183–1208 °C and 0.44–0.46 GPa). On the basis of these results, we modelled the compositional variations of cumulates during cooling and batch crystallization via the rhyolite-MELTS program (Ghiorso and Gualda, 2015) under different pressures (0.3, 0.4 and 0.5 GPa). Plots of the crystallization curves, utilizing MgO and other oxides (Al_2O_3, FeOt, SiO_2 and CaO), indicate the trend of differentiation (Fig. 12). The layered gabbros are consistent with the modelled curves, suggesting that they could have been derived from similar boninitic-like parental magmas by batch crystallization. However, some of isotropic gabbros plot away from these curves, implying that their parental magmas may have been distinctly different from those of the layered gabbros, or that there are additional factors controlling the crystallization.

Trace element concentrations of mafic cumulates are mainly dependent on the fraction of interstitial liquid in the crystal mush, which can be estimated using the methods of Guo et al. (2015). The fraction of the interstitial liquid for the Kızıldağ layered gabbros is estimated to be 3–6 wt%, whereas it is 3–15 wt% for the isotropic gabbros. In addition, the modelling results show that the variations in the partitioning behavior and trace element concentrations of the remaining melts during crystallization were nearly negligible in the estimated pressure range (0.3 to 0.5 GPa). We therefore simulated the trace element compositions of the solid-liquid mixtures with various fractions of interstitial liquid of 3 wt%, 6 wt%, 10 wt% and 15 wt% after 40%, 50%, 60%, 70%, 80% and 90% crystallization under 0.4 GPa (Figs. 13, 14). The results show that the trace element compositions of most layered gabbro samples are consistent with crystallization curves based on interstitial liquid fractions of 3–6 wt% (Fig. 13), whereas the trace elements of the isotropic gabbro samples are similar to the modelling curves produced for higher interstitial liquid fractions (3–15 wt%) (Fig. 14). Hence, the parental magmas of the gabbros could have been boninitic-like magmas in a forearc setting, and the higher trace element concentrations of the isotropic gabbros could be attributed to relatively high fractions of interstitial liquid. This may partly explain why the major element compositions of the isotropic gabbros are distinctly different from the layered gabbros (Fig. 12).

5.6. Petrogenetic model

Variations of parental magmas (from FAB to boninitic) of the sheeted dikes and gabbros of the Kızıldağ ophiolite coupled with the proposed melting depth (35–40 km) are consistent with those in the IBM (Reagan et al., 2010), suggesting that the magmatism occurred during subduction initiation. The subducted oceanic slab was a MORB-type lithosphere fragment created in the southern Tethyan Ocean (Dilek and Thy, 2009). Subduction may have started slowly with a shallow angle up to the point at which initial rapid rollback led to extension and spreading of the upper plate within a protoarc, resulting in formation of FAB dikes/lavas with little subduction input. During this stage, the initial melting mainly

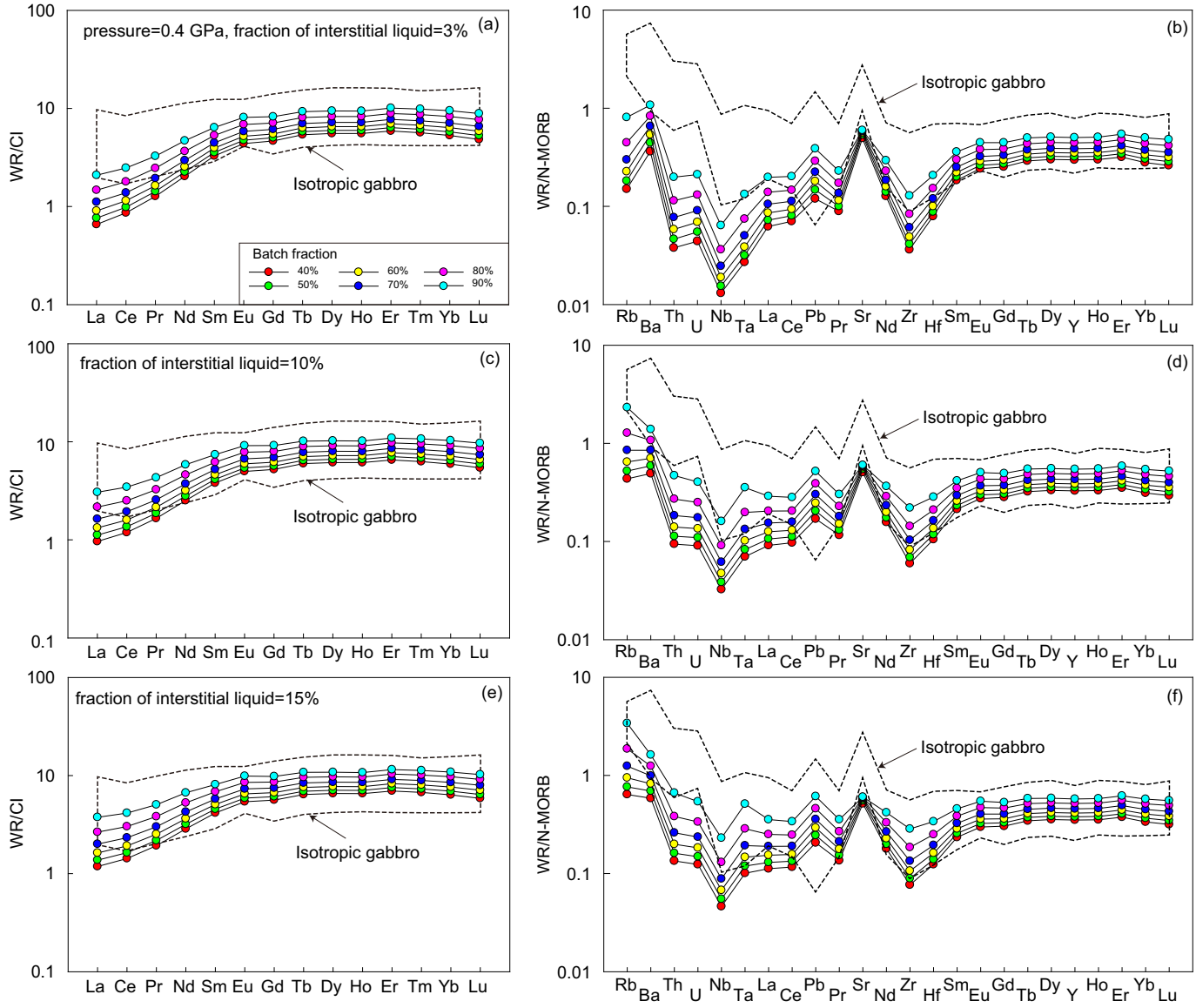

Fig. 14. Batch fractionation models for the Kızıldağ isotropic gabbros are shown on the chondrite-normalized REE (a, c, e) and N-MORB-normalized multi-element (b, d, f) diagrams. Normalization values are from Sun and McDonough (1989). The curves represent the compositions of cumulates through 40%, 50%, 60%, 70%, 80% and 90% crystallization, with different fractions of interstitial liquid (3 wt%, 10 wt% and 15 wt%).

followed a path of polybaric continuous melting (<10%). During sinking of the slab, mafic oceanic crust and sediments were subducted to ever greater depths, where they were dehydrated and/or partially melted, releasing buoyant fluids and/or melts that were easily transported into the overlying mantle wedge. These slab-derived melts/fluids would have depressed the peridotite solidus, and induced flux-melting in the mantle wedge (e.g., Grove et al., 2012). Because the contribution of the subduction component to the mantle wedge was highly variable, the dikes/lavas of the Kızıldağ ophiolite had compositions transitional from FAB to boninitic, and their Pb isotopic compositions straddled the fields from MORB to subducted sediments (Fig. 7). When the ascending magmas were emplaced into the overlying crust, cooling and crystallization of the magmas generated the layered and isotropic gabbros. The isotropic gabbros with higher trace element concentrations contained higher fractions of interstitial liquid during crystallization.

As described above, we propose a semi-quantitative model for the magmatism of the Kızıldağ ophiolite. In order to test whether this model can be applied to other Tethyan ophiolites in the eastern Mediterranean region, we collected data on dikes and lavas for the Lycian, Pozantı-Karsantı (in the Tauride belt) and Troodos (in the Peri-Arabic belt) ophiolites for comparison with the results of our melting models (Fig. 15). The Lycian mafic dikes and lavas plot close to the flux-melting trends of the DMM source (Fig. 15a, b). In contrast, the Pozantı-Karsantı dikes and lavas have trace element concentrations and patterns that plot between the curves of flux-melting of DMM and the DMM after 5% polybaric melting (Fig. 15c, d), suggesting that their parental magmas could have been generated by variable proportions of flux-melting and polybaric continuous melting in the mantle source. The compositions of the Troodos dikes and lavas mostly fit the melting trends of DMM and 10%-depleted DMM sources (Fig. 15e, f), similar to the Kızıldağ ophiolite, suggesting that they may be the integrated products of polybaric melting (<10%) and flux-melting (<25%) of the mantle source. Thus, the petrogenesis of the Kızıldağ mafic rocks may be a viable model for many other Tethyan ophiolites and may provide a blueprint of incipient arc magmatism in subduction zones.

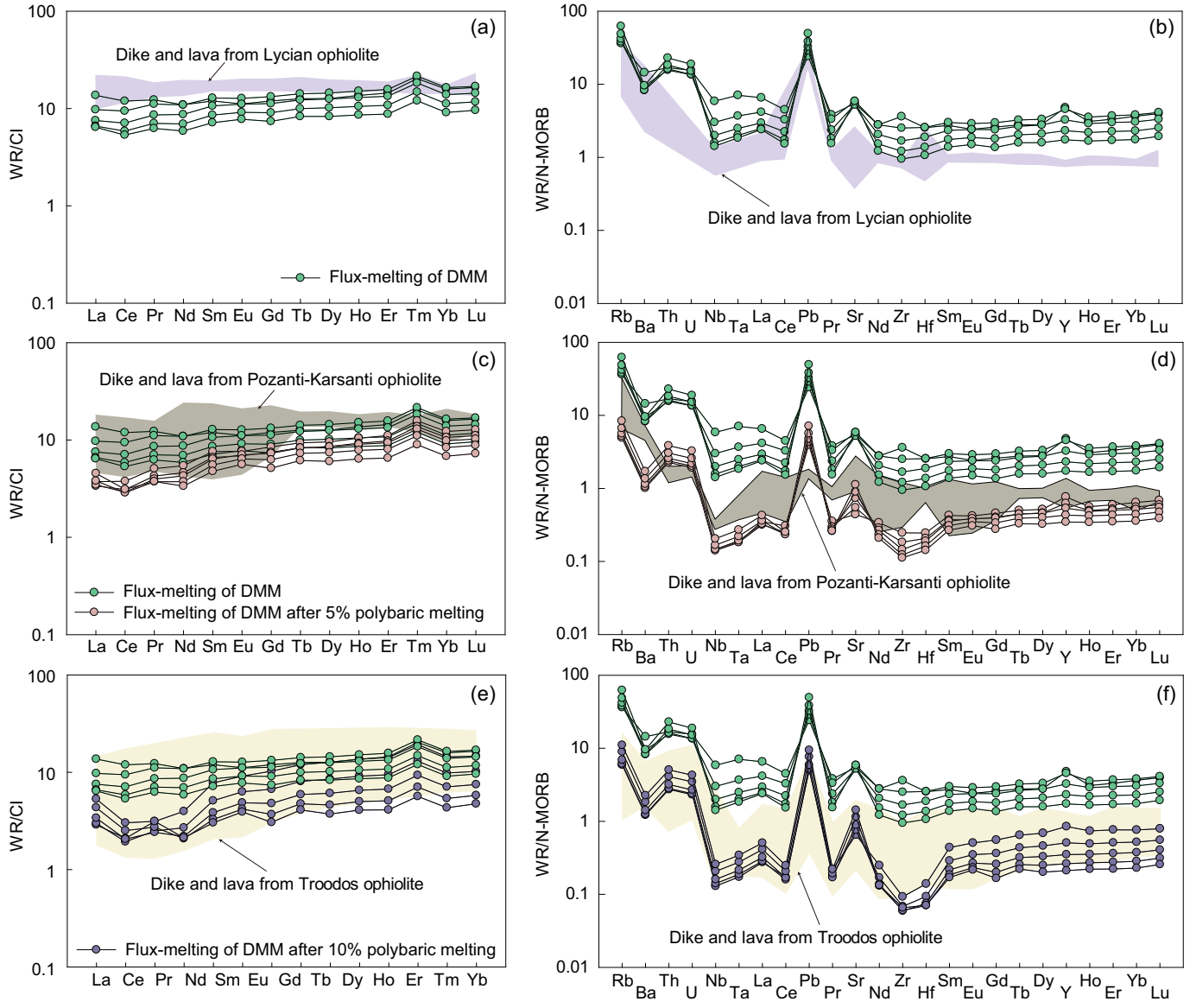

Fig. 15. Partial melting models for the dikes and lavas from the Lycian (a, b), Pozantı-Karsantı (c, d) and Troodos ophiolites (e, f). The geochemical data are from the following source: Lycian (Celik, 2008); Pozantı-Karsantı (Lian et al., 2017; Lytwyn and Casey, 1993; Parlak et al., 2000); Troodos (Cooke et al., 2014; Dilek and Furnes, 2009; Osozawa et al., 2012; Rautenschlein et al., 1985; Taylor, 1987).

6. Conclusions

The geochemical compositions of sheeted dikes and gabbros of the Kızıldağ ophiolite vary from FAB to boninitic and are analogous to those of the IBM. Partial melting in the mantle source of the Kızıldağ ophiolite took place under P-T-fO_2 conditions of ~1 GPa, ~1200–1300 °C and ~ΔFMQ. Such conditions are comparable with the equilibrium thermodynamic conditions of the IBM basalt and boninite, indicating that the evolutionary trend of Kızıldağ developed in a mantle wedge beneath a proto-forearc during subduction initiation. On the basis of polybaric continuous melting and flux-melting models, we conclude that the sheeted dikes may be the integrated products of polybaric continuous melting (<10%) and flux-melting (<25%) of the mantle peridotites. In addition, the major and trace element compositions of the layered gabbros can be well matched with those produced by batch crystallization of boninitic magmas. The isotropic gabbros with higher trace element concentrations could be attributed to higher fractions of interstitial liquid. The two-stage petrogenetic model, which can explain the geochemical diversity of magmas in the Kızıldağ ophiolite, can be also applicable to many other Tethyan ophiolites in the eastern Mediterranean region, such as the Lycian, Pozantı-Karsantı and Troodos ophiolites.

Declaration of Competing Interest

The authors whose names are listed immediately below certify that they have no affiliations with or involvement in any organization or entity with any financial interest (Such as honoraria; educational grants; participation in speakers' bureaus; membership, employment, consultancies, stock ownership, or other equity interest; and expert testimony or patent-licensing arrangements), or non-financial interest (such as personal or professional relationship, affiliations, knowledge or beliefs) in the subject matter or materials discussed in this manuscript.

Acknowledgments

This study was supported by the National Natural Science Foundation of China (grants Nos. 91755205, 41772055 and 91962217). We

thank Paul T. Robinson for English correction, Chang-Ming Xing for the EPMA analysis, Wen-Jun Li for the ICP-MS analysis, and Yan Xiao, Ke-Zhang Qin, Wei Lin and Peng-Fei Zhang for the assistance in the field trips in the Kızıldağ ophiolite.

Appendix A. Supplementary data

Supplementary data to this article can be found online at https://doi.org/10.1016/j.lithos.2021.106348.

References

Aldanmaz, E., Pearce, J.A., Thirlwall, M.F., Mitchell, J.G., 2000. Petrogenetic evolution of late Cenozoic, post-collision volcanism in western Anatolia, Turkey. J. Volcanol. Geotherm. Res. 102, 67–95.

Asimow, P.D., Hirschmann, M.M., Stolper, E.M., 2001. Calculation of peridotite partial melting from thermodynamic models of minerals and melts, IV. adiabatic decompression and the composition and mean properties of mid-ocean ridge basalts. J. Petrol. 42, 963–998.

Bagci, U., Parlak, O., Höck, V., 2005. Whole-rock and mineral chemistry of cumulates from the Kızıldağ (Hatay) ophiolite (Turkey): clues for multiple magma generation during crustal accretion in the southern Neotethyan Ocean. Mineral. Mag. 69, 53–76.

Bagci, U., Parlak, O., Höck, V., 2008. Geochemistry and tectonic environment of diverse magma generations forming the crustal units of the Kızıldağ (Hatay) ophiolite, Southern Turkey. Turk. J. Earth Sci. 17, 43–71.

Beccaluva, L., Macciotta, G., Piccardo, G.B., Zeda, O., 1989. Clinopyroxene composition of ophiolite basalts as petrogenetic indicator. Chem. Geol. 77, 165–182.

Beccaluva, L., Coltorti, M., Giunta, G., Siena, F., 2004. Tethyan vs. Cordilleran ophiolites: a reappraisal of distinctive tectono-magmatic features of supra-subduction complexes in relation to the subduction mode. Tectonophysics 393, 163–174.

Behn, M.D., Kelemen, P.B., Hirth, G., Hacker, B.R., Massonne, H.J., 2011. Diapirs as the source of the sediment signature in arc lavas. Nat. Geosci. 4, 641–646.

Bingol, A.F., Beyarslan, M., Lin, Y.C., Lee, H.Y., 2018. Geochronological and geochemical constraints on the origin of the southeast Anatolian ophiolites, Turkey. Arab. J. Geosci. 11, 569.

Blundy, J., Wood, B., 1994. Prediction of crystal-melt partition-coefficients from Elastic-Moduli. Nature 372, 452–454.

Burns, L.E., 1985. The Border Ranges ultramafic and mafic complex, south-Central Alaska: cumulate fractionates of island-arc volcanics. Can. J. Earth Sci. 22, 1020–1038.

Celik, O.F., 2008. Detailed geochemistry and K-Ar geochronology of the metamorphic sole rocks and their mafic dykes from the Mersin ophiolite, southern Turkey. Turk. J. Earth Sci. 17, 685–708.

Chen, C., Su, B.X., Uysal, İ., Avci, E., Zhang, P.F., Xiao, Y., He, Y.S., 2015. Iron isotopic constraints on the origin of peridotite and chromitite in the Kızıldağ ophiolite, southern Turkey. Chem. Geol. 417, 115–124.

Chen, C., Su, B.X., Jing, J.J., Xiao, Y., Lin, W., Chu, Y., Liu, X., Bai, Y., 2018. Geological records of subduction initiation of Neo-Tethyan Ocean: ophiolites and metamorphic soles in southern Turkey. Acta Petrol. Sin. 34, 3302–3314 (in Chinese with English abstract).

Chen, C., Su, B.X., Xiao, Y., Pang, K.N., Robinson, P.T., Uysal, I., Lin, W., Qin, K.Z., Avci, E., Kapsiotis, A., 2019. Intermediate chromitite in Kizildag ophiolite (SE Turkey) formed during subduction initiation in Neo-Tethys. Ore Geol. Rev. 104, 88–100.

Condie, K.C., 2005. High field strength element ratios in Archean basalts: a window to evolving sources of mantle plumes? Lithos 79, 491–504.

Cooder, J.A., Wiens, D.A., Morris, J., 2002. On the decompression melting strcture at volcanic arcs and back-arc spreading centers. Geophys. Res. Lett. 29, 1727.

Cooke, A.J., Masson, L.P., Robertson, A.H.F., 2014. Construction of a sheeted dyke complex: evidence from the northern margin of the Troodos ophiolite and its southern margin adjacent to the Arakapas Fault Zone. Ofioliti 39, 1–30.

Dilek, Y., Flower, M.F.J., 2003. Arc-trench rollback and forearc accretion: 2. A model template for ophiolites in Albania, Cyprus, and Oman. Geol. Soc. Lond., Spec. Publ. 218, 43–68.

Dilek, Y., Furnes, H., 2009. Structure and geochemistry of Tethyan ophiolites and their petrogenesis in subduction rollback systems. Lithos 113, 1–20.

Dilek, Y., Furnes, H., 2019. Tethyan ophiolite and Tethyan seaways. J. Geol. Soc. 176, 899–912.

Dilek, Y., Moores, E.M., 1990. Regional tectonics of the eastern Mediterranean ophiolites. In: Troodos 1987. Symposium, pp. 295–309.

Dilek, Y., Thy, P., 1998. Structure, petrology, and seafloor spreading tectonics of the Kızıldağ ophiolite, Turkey. In: Mills, R.A., Harrison, K. (Eds.), Modern Ocean Floor Processes and the Geological Record: Geological Society of London Special Publication, 148, pp. 43–69.

Dilek, Y., Thy, P., 2009. Island arc tholeiite to boninitic melt evolution of the cretaceous Kızıldağ (Turkey) ophiolite: model for multi-stage early arc-forearc magmatism in Tethyan subduction factories. Lithos 113, 68–87.

Dilek, Y., Shallo, M., Furnes, H., 2005. Rift-drift, seafloor spreading, and subduction tectonics of Albanian ophiolites. Int. Geol. Rev. 47, 147–176.

Dilek, Y., Furnes, H., Shallo, M., 2007. Suprasubduction zone ophiolite formation along the periphery of Mesozoic Gondwana. Gondwana Res. 11, 453–475.

Dilek, Y., Furnes, H., Shallo, M., 2008. Geochemistry of the Jurassic Mirdita Ophiolite (Albania) and the MORB to SSZ evolution of a marginal basin oceanic crust. Lithos 100, 174–209.

Elitok, O., 2012. Geology, geochemistry and geodynamic implications of the mafic-ultramafic rocks from the northern part of the Antalya complex, SE Turkey. Tectonophysics 568, 335–356.

Ghiorso, M.S., Gualda, G.A.R., 2015. An H_2O-CO_2 mixed fluid saturation model compatible with rhyolite-MELTS. Contrib. Mineral. Petrol. 169, 1–30.

Gibson, I.L., Kirkpatrick, R.J., Emmerman, R., Schmincke, H.U., Pritchard, G., Oakley, P. J., Thorpe, R.S., Marriner, G.F., 1982. The trace element composition of the lavas and dikes from a 3-km vertical section through the lava pile of eastern Iceland. J. Geophys. Res. Solid Earth 87, 6532–6546.

Gifkins, C.C., Herrmann, W., Large, R.R., 2005. Altered Volcanic Rocks: A Guide to Description and Interpretation. University of Tasmania, Centre for Ore Deposit Research.

Godard, M., Bosch, D., Einaudi, F., 2006. A MORB source for low-Ti magmatism in the Semail ophiolite. Chem. Geol. 234, 58–78.

Grove, T., Parman, S., Bowring, S., Price, R., Baker, M., 2002. The role of an H_2O-rich fluid component in the generation of primitive basaltic andesites and andesites from the Mt. Shasta region, N California. Contrib. Mineral. Petrol. 142, 375–396.

Grove, T.L., Till, C.B., Krawczynski, M.J., 2012. The role of H_2O in subduction zone magmatism. Annu. Rev. Earth Planet. Sci. 40, 413–439.

Guo, F., Li, H.X., Fan, W.M., Li, J.Y., Zhao, L., Huang, M.W., Xu, W.L., 2015. Early Jurassic subduction of the Paleo-Pacific Ocean in NE China: petrologic and geochemical evidence from the Tumen mafic intrusive complex. Lithos 224, 46–60.

Hart, S.R., 1984. A large-scale isotope anomaly in the Southern Hemisphere mantle. Nature 309, 753–757.

Hawkins, J.W., Bloomer, S.H., Evans, C.A., Melchior, J.T., 1984. Evolution of intra-oceanic arc-trench systems. Tectonophysics 102, 175–205.

Ishikawa, T., Kazuya, N., Susumu, U., 2002. Boninitic volcanism in the Oman ophiolite: Implications for thermal condition during transition from spreading ridge to arc. Geology 30, 899–902.

Jayasuriya, K.D., O'Neill, H.S.C., Berry, A.J., Campbell, S.J., 2004. A Mössbauer study of the oxidation state of Fe in silicate melts. Am. Mineral. 89, 1597–1609.

Kakar, M.I., Mahmood, K., Arif, M., Khan, M., Kerr, A.C., Mohibullah, M., Kasi, A.K., 2015. Petrology and geochemistry of mafic dykes from the Muslim Bagh ophiolite (Pakistan): implications for petrogenesis and emplacement. Turk. J. Earth Sci. 24, 165–178.

Karaoğlan, F., Parlak, O., Klötzli, U., Thöni, M., Koller, F., 2013. U-Pb and Sm-Nd geochronology of the Kızıldağ (Hatay, Turkey) ophiolite: implications for the timing and duration of suprasubduction zone type oceanic crust formation in the southern Neotethys. Geol. Mag. 150, 283–299.

Katz, R.F., Spiegelman, M., Langmuir, C.H., 2003. A new parameterization of hydrous mantle melting. Geochem. Geophys. Geosyst. 4.

Kelemen, P.B., Nobumichi, S., Vincent, J.M.S., 1995. Extraction of mid-ocean-ridge basalt from the upwelling mantle by focused flow of melt in dunite channels. Nature 375, 747–753.

Khedr, M.Z., Arai, S., Python, M., Tamura, A., 2014. Chemical variations of abyssal peridotites in the Central Oman ophiolite: evidence of oceanic mantle heterogeneity. Gondwana Res. 25, 1242–1262.

Kimura, J.I., 2017. Modeling chemical geodynamics of subduction zone using the arc basalt simulator version 5. Geosphere 13, 992–1025.

Kohut, E.J., Stern, R.J., Kent, A.J.R., Nielsen, R.L., Bloomer, S.H., Levbourne, M., 2006. Evidence for adiabatic decompression melting in the Southern Mariana Arc from high-Mg lavas and melt inclusions. Contrib. Mineral. Petrol. 152, 201–221.

Lee, C.-T.A., Luffi, P., Plank, T., Dalton, H., Leeman, W.P., 2009. Constraints on the depth and temperatures of basaltic magma generation on Earth and other terrestrial planets using new thermobarometers for mafic magmas. Earth Planet. Sci. Lett. 279, 20–33.

Lee, C.-T.A., Luffi, P., Chin, E.J., Bouchet, R., Dasgupta, R., Morton, D.M., Le Roux, V., Yin, Q.Z., Jin, D., 2012. Copper systematics in arc magmas and implications for crust-mantle differentiation. Science 336, 64–68.

Li, C.F., Chu, Z.Y., Guo, J.H., Li, Y.L., Yang, Y.H., Li, X.H., 2015. A rapid single column separation scheme for high-precision Sr-Nd-Pb isotopic analysis in geological samples using thermal ionization mass spectrometry. Anal. Methods 7, 4793–4802.

Li, H.Y., Taylor, R.N., Prytulak, J., Kirchenbaur, M., Shervais, J.W., Ryan, J.G., Godard, M., Reagan, M.K., Pearce, J.A., 2019. Radiogenic isotopes document the start of subduction in the Western Pacific. Earth Planet. Sci. Lett. 518, 197–210.

Lian, D.Y., Yang, J.S., Dilek, Y., Liu, F., Wu, W.W., Xiong, F.H., 2017. Geochemical, geochronological, and Sr-Nd isotopic constraints on the origin of the mafic dikes from the Pozanti-Karsanti ophiolite: Implications for tectonic evolution. J. Geol. 125.

Lytwyn, J.N., Casey, J.F., 1993. The geochemistry and petrogenesis of volcanics and sheeted dikes from the Hatay (Kızıldağ) ophiolite, southern Turkey: possible formation with the Troodos ophiolite, Cyprus, along fore-arc spreading centers. Tectonophysics 223, 237–272.

Mathieu, L., 2018. Quantifying hydrothermal alteration: a review of methods. Geosciences 8, 245.

McKenzie, D., O'Nions, R.K., 1991. Partial melt distributions from inversion of rare-earth element concentrations. J. Petrol. 32, 1021–1091.

McKenzie, D., O'Nions, R.K., 1995. The source regions of ocean island basalts. J. Petrol. 36, 133–159.

Osozawa, S., Shinjo, R., Lo, C.H., Jahn, B.M., Hoang, N., Sasaki, M., Ishikawa, K., Kano, H., Hoshi, H., Xenophontos, C., Wakabayashi, J., 2012. Geochemistry and geochronology of the Troodos ophiolite: an SSZ ophiolite generated by subduction initiation and an extended episode of ridge subduction? Lithosphere 4, 497–510.

Parlak, O., Delaloye, M., Bingol, E., 1996. Mineral chemistry of ultramafic and mafic cumulates as an indicator of the arc-related origin of the Mersin ophiolite (southern Turkey). Geol. Rundsch. 85, 647–661.
Parlak, O., Hock, V., Delaloye, M., 2000. Suprasubduction zone origin of the Pozanti-Karsanti ophiolite (southern Turkey) deduced from whole-rock and mineral chemistry of the gabbroic cumulates. Geol. Soc. Lond., Spec. Publ. 173, 219–234.
Parlak, O., Hock, V., Delaloye, M., 2002. The supra-subduction zone Pozanti-Karsanti ophiolite, southern Turkey: evidence for high-pressure crystal fractionation of ultramafic cumulates. Lithos 65, 204–224.
Pearce, J.A., 1996. A user's guide to basalt discrimination diagrams. Trace element geochemistry of volcanic rocks: applications for massive sulphide exploration. Geol. Assoc. Canada Short Course Notes 12, 79–113.
Pearce, J.A., 2008. Geochemical fingerprinting of oceanic basalts with applications to ophiolite classification and the search for Archean oceanic crust. Lithos 100, 14–48.
Pearce, J.A., 2014. Immobile element fingerprinting of ophiolites. Elements 10, 101–108.
Pearce, J.A., Parkinson, I.J., 1993. Trace element models for mantle melting: application to volcanic arc petrogenesis. Geol. Soc. Lond., Spec. Publ. 76, 373–403.
Piskin, O., Delaloye, M., Moritz, R., Wagner, J.J., 1990. Geochemistry and geothermometry of the Hatay Complex Turkey: implications for the genesis of the ophiolite sequence. In: Ophiolites, Malpas J. (Ed.), Oceanic Crustal Analogues: Proceedings of the Symposium "Troodos 1987", pp. 329–338.
Plank, T., Kelley, K.A., Zimmer, M.M., Hauri, E.H., Wallace, P.J., 2013. Why do mafic arc magmas contain ~4 wt% water on average? Earth Planet. Sci. Lett. 364, 169–179.
Putirka, K.D., 2008. Thermometers and barometers for volcanic systems. Rev. Mineral. Geochem. 69, 61–120.
Qiu, X.F., Ling, W.L., Liu, X.M., Kusky, T., Berkana, W., Zhang, Y.H., Gao, Y.J., Lu, S.S., Kuang, H., Liu, C.X., 2011. Recognition of Grenvillian volcanic suite in the Shennongjia region and its tectonic significance for the South China Craton. Precambrian Res. 191, 101–119.
Rautenschlein, M., Jenner, G.A., Hertogen, J., Hofmann, A.W., Kerrich, R., Schmincke, H. U., White, W.M., 1985. Isotopic and trace element composition of volcanic glasses from the Akaki Canyon, Cyprus: implications for the origin of the Troodos ophiolite. Earth Planet. Sci. Lett. 75, 369–383.
Reagan, M.K., Ishizuka, O., Stern, R.J., Kelley, K.A., Ohara, Y., Blichert-Toft, J., Bloomer, S.H., Cash, J., Fryer, P., Hanan, B.B., Hickey-Vargas, R., Ishii, T., Kimura, J. I., Peate, D.W., Rowe, M.C., Wood, M., 2010. Fore-arc basalts and subduction initiation in the Izu-Bonin-Mariana system. Geochem. Geophys. Geosyst. 11, 1–17.
Ricou, L.E., Marcoux, J., Whitechurch, H., 1984. The Mesozoic organization of the Taurides: one or several ocean basins. Geol. Soc. Lond., Spec. Publ. 17, 349–359.
Robertson, A.H.F., 2002. Overview of the genesis and emplacement of Mesozoic ophiolites in the eastern Mediterranean Tethyan region. Lithos 65, 1–67.
Saccani, E., Allahyari, K., Rahimzadeh, B., 2014. Petrology and geochemistry of mafic magmatic rocks from the Sarve-Abad ophiolites (Kurdistan region, Iran): evidence for interaction between MORB-type asthenosphere and OIB-type components in the southern Neo-Tethys Ocean. Tectonophysics 621, 132–147.
Sayit, K., Marroni, M., Concuoglu, M.C., Pandolfi, L., Ellero, A., Ottria, G., Frassi, C., 2016. Geological setting and geochemical signatures of the mafic rocks from the Intra-Pontide Suture Zone: implications for the geodynamic reconstruction of the Mesozoic Neotethys. Int. J. Earth Sci. 105, 39–64.
Shervais, J.W., 1982. Ti-V plots and the petrogenesis of modern and ophiolitic lavas. Earth Planet. Sci. Lett. 59, 101–118.
Shervais, J.W., Reagan, M., Haugen, E., Almeev, R.R., Pearce, J.A., Prytulak, J., Ryan, J. G., Whattam, S.A., Godard, M., Chapman, T., Li, H.Y., Kurz, W., Nelson, W.R., Heaton, D., Kirchenbaur, M., Shimizu, K., Sakuyama, T., Li, Y.B., Vetter, S.K., 2019. Magmatic response to subduction initiation: Part I. fore-arc basalts of the Izu-Bonin arc from IODP expedition 352. Geochem. Geophys. Geosyst. 20.
Smith, P.M., Asimow, P.D., 2005. Adiabat_1ph: a new public front-end to the MELTS, pMELTS, and pHMELTS models. Geochem. Geophys. Geosyst. 6.
Stern, R.J., 2002. Subduction zones. Rev. Geophys. 40.
Su, B.X., Robinson, P.T., Chen, C., Xiao, Y., Melcher, F., Bai, Y., Gu, X.Y., Uysal, I., Lenaz, D., 2020. The occurrence, origin, and fate of water in chromitites in ophiolites. Am. Mineral. 105, 894–903.
Sun, S.S., McDonough, W.F., 1989. Chemical and isotopic systematics of oceanic basalts: implications for mantle composition and processes. Geol. Soc. Lond., Spec. Publ. 42, 313–345.
Tatsumi, Y., Eggins, S., 1995. Subduction Zone Magmatism, 224 P. Blackwell Science, Cambridge, Massachusetts.
Taylor, R.N., 1987. Geochemical stratigraphy of the Troodos extrusive sequence: temporal developments of a spreading centre magma chamber. In: Ophiolites, Oceanic Crustal Analogues. Proceedings of the Symposium, pp. 173–183.
Tinkler, C., Wagner, J.J., Delaloye, M., Selcuk, H., 1981. Tectonic history of the Hatay ophiolites (South Turkey) and their relation with the Dead Sea Rift. Tectonophysics 72, 23–41.
Uysal, İ., Kapsiotis, A., Akmaz, R.M., Saka, S., Seitz, H.M., 2018. The Guleman ophiolitic chromitites (SE Turkey) and their link to a compositionally evolving mantle source during subduction initiation. Ore Geol. Rev. 93, 98–113.
Van Keken, P.E., 2003. The structure and dynamics of the mantle wedge. Earth Planet. Lett. 215, 323–338.
Woelki, D., Regelous, M., Haase, K.M., Romer, R.H.W., Beier, C., 2018. Petrogenesis of boninitic lavas from the Troodos ophiolite, and composition with Izu-Bonin-Mariana fore-arc crust. Earth Planet. Sci. Lett. 498, 203–214.
Wood, B.J., Blundy, J.D., 1997. A predictive model for rare earth element partitioning between clinopyroxene and anhydrous silicate melt. Contrib. Mineral. Petrol. 129, 166–181.
Workman, R.K., Hart, S.R., 2005. Major and trace element composition of the depleted MORB mantle (DMM). Earth Planet. Sci. Lett. 231, 53–72.
Yao, Z.S., Qin, K.Z., Mungall, J.E., 2018. Tectonic controls on Ni and Cu contents of primary mantle-derived magmas for the formation of magmatic sulfide deposits. Am. Mineral. 103, 1545–1567.